A VLT VIMOS study of the anomalous BCD Mrk 996: mapping the ionized gas kinematics and abundances

Mon. Not. R. Astron. Soc. **398,** 2–22 (2009) doi:10.1111/j.1365-2966.2009.15172.x

A VLT VIMOS study of the anomalous BCD Mrk 996: mapping the ionized gas kinematics and abundances⋆

B. L. James,[1]† Y. G. Tsamis,[1,2]† M. J. Barlow,[1] M. S. Westmoquette,[1] J. R. Walsh,[3] F. Cuisinier[4] and K. M. Exter[5]

[1]*Department of Physics and Astronomy, University College London, Gower Street, London WC1E 6BT*
[2]*Instituto de Astrofísica de Andalucía (CSIC), Apartado 3004, 18080 Granada, Spain*
[3]*Space Telescope European Co-ordinating Facility, European Southern Observatory, Karl-Schwarzschild Strasse 2, D-85748 Garching, Germany*
[4]*GEMAC – Departamento de Astronomia/Observatório do Valongo, Universidade Federal do Rio de Janeiro, Ladeira do Pedro Antonio 43, 20080-090 Rio de Janeiro, RJ, Brazil*
[5]*Inst. voor Sterrenkunde, Celestijnenlaan 200D BUS 2401, 3001 Heverlee, Leuven, Belgium*

Accepted 2009 May 25. Received 2009 April 10; in original form 2008 December 18

ABSTRACT

A study of the blue compact dwarf (BCD) galaxy Mrk 996 based on high-resolution optical Very Large Telescope Visible Multi-Object Spectrograph integral field unit spectroscopy is presented. Mrk 996 displays multicomponent line emission, with most line profiles consisting of a narrow, central Gaussian [full width at half-maximum (FWHM) $\sim 110\,\mathrm{km\,s^{-1}}$] with an underlying broad component (FWHM $\sim 400\,\mathrm{km\,s^{-1}}$). The broad H I Balmer component splits into two separate broad components inside a 1.5-arcsec radius from the nucleus; these are attributed to a two-armed minispiral. This spiral-like nucleus rotates in the same sense as the extended narrow line ionized gas but is offset by $\sim$50 km s^{-1} from the systemic velocity of the galaxy. The rotation curve of Mrk 996 derived from the Hα narrow component yields a total mass of $5 \times 10^8\,\mathrm{M_\odot}$ within a radius of 3 kpc. From the Hα luminosity we infer a global star formation rate of $\sim 2\,\mathrm{M_\odot\,yr^{-1}}$.

The high excitation energy, high critical density [O III] λ4363 and [N II] λ5755 lines are only detected from the inner region and exist purely in broad component form, implying unusual excitation conditions. Surface brightness, radial velocity and FWHM maps for several emission components are presented. A separate physical analysis of the broad and narrow emission line regions is undertaken. We derive an upper limit of 10 000 K for the electron temperature of the narrow line gas, together with an electron density of $170\,\mathrm{cm^{-3}}$, typical of normal H II regions. For the broad line component, measured [O III] and [Fe III] diagnostic line ratios are consistent with a temperature of 11 000 K and an electron density of $10^7\,\mathrm{cm^{-3}}$. The broad line emission regions show N/H and N/O enrichment factors of $\sim$20 relative to the narrow line regions, but no He/H, O/H, S/H or Ar/H enrichment is inferred. Previous studies indicated that Mrk 996 showed anomalously high N/O ratios compared with BCDs of a similar metallicity. Our multicomponent analysis yields a revised metallicity of $\geq 0.5\,\mathrm{Z_\odot}$ ($12 + \log \mathrm{O/H} = 8.37$) for both the narrow and broad gas components, significantly higher than previous studies. As a result the narrow line region's N/O ratio is now typical for the galaxy's metallicity. The narrow line component's N/O ratio peaks outside the core region, spatially correlating with $\sim$3-Myr-old stellar populations. The dominant line excitation mechanism is photoionization by the $\sim$3000 Wolf–Rayet stars and $\sim$150 000 O-type stars estimated to be present in the core. This is indeed a peculiar BCD, with extremely dense zones of gas in the

⋆Based on observations made with ESO telescopes at the Paranal Observatory under programme ID 078.B-0353(A).
†E-mail: bj@star.ucl.ac.uk (BLJ); tsamis@iaa.es (YGT)

core, through which stellar outflows and possible shock fronts permeate contributing to the excitation of the broad line emission.

Key words: stars: Wolf–Rayet – galaxies: abundances – galaxies: dwarf – galaxies: individual: Markarian 996 – galaxies: kinematics and dynamics – galaxies: starburst.

1 INTRODUCTION

Blue compact dwarf (BCD) galaxies provide a means of studying chemical evolution and star formation in low metallicity environments in the nearby Universe. In general BCDs are faint ($M_B > 18$), have blue optical colours, are typically small ($\lesssim$1 kpc) and are thought to be experiencing bursts of star formation in relatively chemically unevolved environments, ranging from 1/2 to 1/50 solar metallicity (Kunth & Östlin 2000), and are therefore good analogues to high-redshift star-forming galaxies (SFG).

The current study focuses on Markarian 996, a BCD whose properties are far from ordinary. Thuan, Izotov & Lipovetsky (1996, hereafter TIL96) presented a comprehensive *Hubble Space Telescope* (*HST*) study of Mrk 996 by analysing Faint Object Spectrograph (FOS) ultraviolet (UV) and optical spectra and Wide-Field Planetary Camera 2 (WFPC2) *V*- and *I*-band imaging. Their *HST* *V*-band image, shown in Fig. 1, revealed that the majority of the star formation in Mrk 996 occurs within a bright, compact nuclear H II region of ∼3 arcsec angular radius (∼315 pc for their adopted distance of 21.6 Mpc; TIL96) surrounded by an extended elliptical low surface brightness component of ∼40.6-arcsec diameter. However, the remarkable nature of the galaxy was exposed by the small-aperture (∼1 arcsec) FOS spectra obtained from the nucleus of Mrk 996. Linewidths increase with the degree of ionization; lines from singly ionized species being narrow and typical of H II regions whereas lines from ions such as O^{2+} and Ne^{2+} are very broad, with full width at half-maximum (FWHM) widths up to ∼900 km s^{-1} (TIL96). Unphysically high [O III] electron temperatures are derived for the nucleus unless an electron density (N_e) of at least $\sim10^6$ cm^{-3} is adopted, several orders of magnitude higher than normal H II region electron densities (Izotov, Thuan & Lipovetsky 1994). In order to account for the observed line intensities, TIL96 applied a two-zone density-bounded H II region model, with an inner core density of $\sim10^6$ cm^{-3} and an outer zone with a density of ∼450 cm^{-3}. They suggested that this large density gradient is caused by a mass outflow driven by the large population of Wolf–Rayet (WR) stars found to be present in the galaxy.

Elemental abundances were also derived by TIL96, who estimated a metallicity of 0.22 $Z_\odot$, based on the abundance of oxygen. As a result of their study, Mrk 996 was placed in a small group of eight BCDs known to display a significant overabundance of nitrogen (Pustilnik et al. 2004), with derived N/O ratios that are 0.3–1.4 dex higher than for other BCDs of similar oxygen abundances. The enhanced nitrogen within this group has been suggested by Pustilnik et al. (2004) to be connected with merger events, in particular with a short phase of the consequent starburst (SB), when many WR stars contribute to the enrichment of the interstellar medium (ISM). This was certainly the case for NGC 5253 (thought to be interacting with its companion galaxy NCG 5236; Moorwood & Glass 1982), where spatially resolved N/H and N/O enhancements were observed by Walsh & Roy (1987) to correlate strongly with WR star signatures. In support of this, a correlation was also found between spatial enhancements of He/H and N/O, attributed to helium enrichment of the ISM by WR stars (Walsh & Roy 1989).

The study of TIL96 showed that Mrk 996 has spatially varying physical properties. Spatially resolved kinematic and chemical abundance information across the galaxy is therefore crucial for understanding the nature of this system; such information can be readily obtained with integral field spectroscopy (IFS). In this paper we present high-resolution optical IFS observations obtained with the Visible Multi-Object Spectrograph (VIMOS) integral field unit (IFU) on the 8.2-m Very Large Telescope (VLT) UT3/Melipal. The data afford us a new spatiokinematic three-dimensional ('3D') view of Mrk 996. The spatial and spectral resolution achieved allows us to undertake a full multivelocity-component analysis of this system, ultimately providing a more complete picture of its diverse ionized ISM.

We adopt a distance of 22.3 Mpc for Mrk 996, at a redshifted velocity of 1642 km s^{-1} (corresponding to $z = 0.00544$, this work), using a Hubble constant $H_0 = 73.5$ km s^{-1} Mpc^{-1} (DeBernardis et al. 2008).

2 VIMOS IFU OBSERVATIONS AND DATA REDUCTION

2.1 Observations

Two data sets were obtained with the VIMOS IFU at the 8.2-m VLT at ESO's Paranal Observatory in Chile. The VIMOS IFU consists of 6400 (80 × 80) fibres coupled to microlenses and operates with four CCD detectors yielding four spectral and spatial quadrant samplings (Zanichelli et al. 2005). The spatial sampling is contiguous, with the dead space between fibres below 10 per cent of the interfibre distance. The data sets were taken with the high resolution and high magnification (i.e. a partially masked IFU head containing only 40 × 40 fibres) settings of the IFU, resulting in a field-of-view (FoV) of 13 × 13 arcsec^2 covered by 1600 spatial pixels (spaxels) at a spatial sampling of 0.33 arcsec per spaxel. Two different grisms were used, high-resolution blue (HRblue, ∼0.51 Å pixel^{-1}), covering 4150–6200 Å and high-resolution orange (HRorange, ∼0.60 Å pixel^{-1}) covering 5250–7400 Å; spectra from both grisms are illustrated in Fig. 2. The instrumental width delivered by the IFU HRblue and HRorange grisms was measured using arc lamp exposures. Gaussian profiles were fitted to a number of isolated lines within each extracted arc spectrum and were found to have FWHMs of 2.3 ± 0.1 Å (113.5 ± 4.9 km s^{-1}) and 1.5 ± 0.1 Å (72.3 ± 4.8 km s^{-1}) for the HRblue and HRorange grisms, respectively.

The observing log can be found in Table 1. Four exposures were taken per grism. The third exposure within each set was dithered by $+0\overset{s}{.}34$ in RA and by $+0''.58$ in Dec. (corresponding to a 2 spaxel offset in the *X*-direction) in order to remove any dead fibres when averaging exposures. All observations were taken at a position angle (PA) of $+30^\circ$.

2.2 Data reduction

The data reduction was carried out using the GUI-based pipeline software GASGANO[1] that allows the user to organize calibration files and run pipeline tasks. Three main tasks were used: (1) VMBIAS

[1] http://www.eso.org/sci/data-processing/software/gasgano

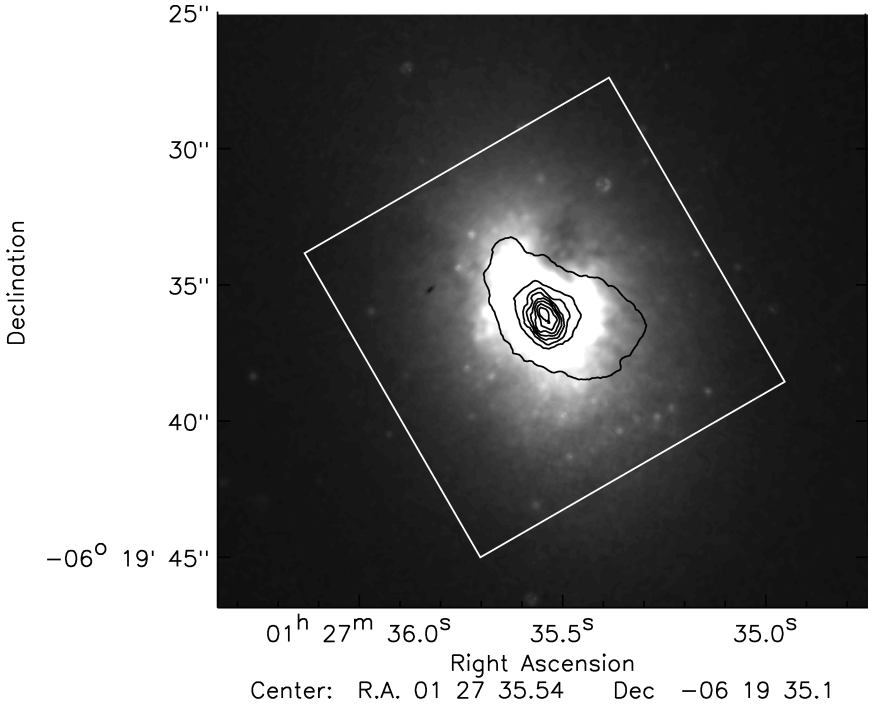

Figure 1. *HST* F569W WFPC2 image of Mrk 996 overlaid with the 13 × 13 arcsec^2 VIMOS IFU aperture at a PA of 30°, along with contours from the VIMOS IFU Hα narrow component emission line map (see Fig. 4). North is up and east is to the left. Hα contours are shown for the range 24.8–899.9, in steps of 119, in surface brightness units of $\times 10^{-15}$ erg cm^{-2} s^{-1} arcsec^{-2}.

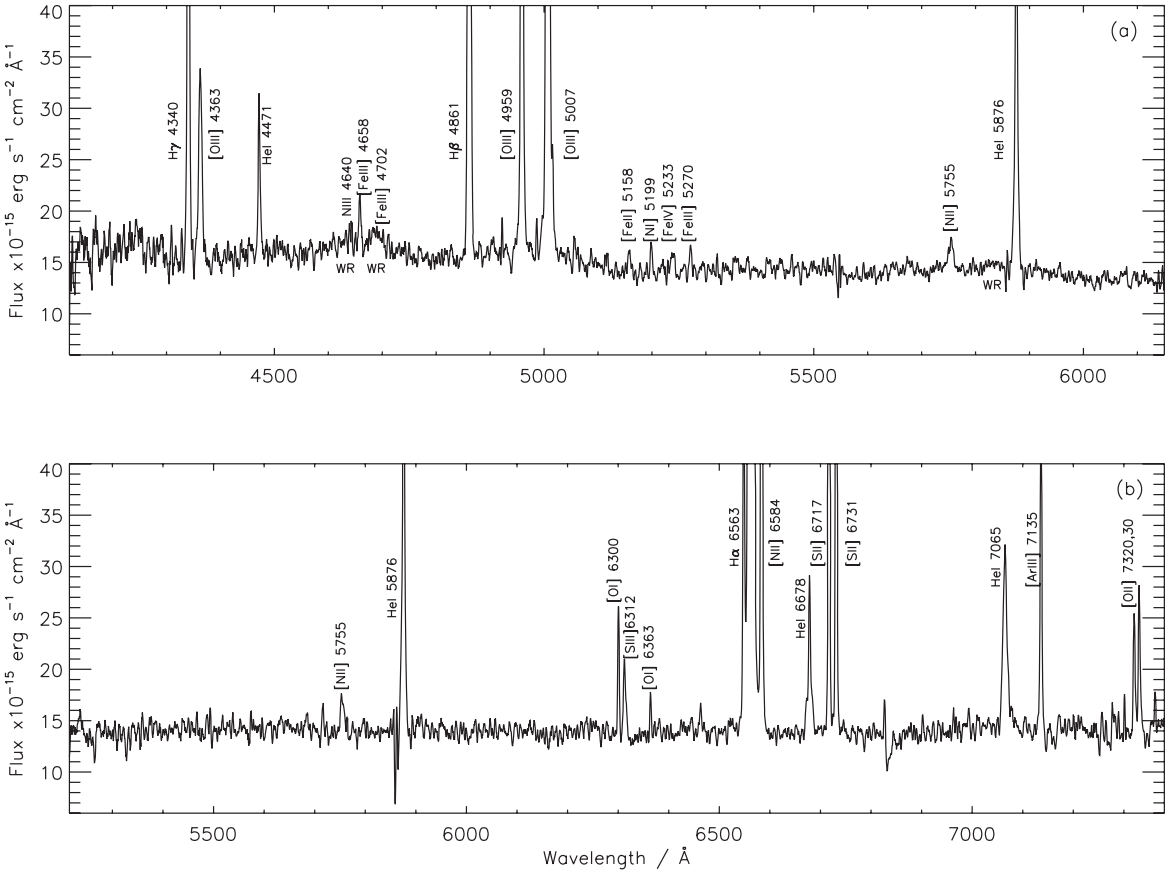

Figure 2. VIMOS IFU summed spectra of Mrk 996 after smoothing with a 5 pixel boxcar: (a) high-resolution blue spectrum; (b) high-resolution orange spectrum. Spectra are integrated over an area of 5.3 × 6.3 arcsec^2 (575 × 685 pc^2) and correspond to exposure times of 4 × 402 and 4 × 372 s for the HR blue and HR orange grisms, respectively.

Table 1. VIMOS IFU observing log.

Observation ID	Date	Grism	Exp. time (s)	Airmass range	FWHM seeing (arcsec)
250520	2006 October 13	HR blue	4 × 402	1.135–1.097	0.72
250516	2006 October 19	HR orange	4 × 372	1.057–1.053	1.15

created the master bias frame; (2) VMIFUCALIB determined the spectral extraction mask, wavelength calibration and the relative fibre transmission correction; (3) VMIFUSTANDARD created flux response curves from a summed spectrophotometric standard star spectrum. Finally, the products of these tasks were fed into VMIFUSCIENCE which extracted the bias-subtracted, wavelength- and flux-calibrated, and relative fibre transmission-corrected science spectra. Each VIMOS CCD quadrant is an independent spectrograph, therefore, the IFU data processing was performed separately on each quadrant, creating four fully calibrated 3D arrays per science exposure. The flux calibration was performed by multiplying the two-dimensional (2D) spectral frame for each quadrant by its relative response curve, derived from standard star observations in the same filter, grism and quadrant. The final data cube is produced by median-combining each exposure in a jitter sequence (i.e. re-aligning the dithered exposure with the other exposures of identical pointing), after all the individual data quadrants for each exposure had been reduced. Reconstructing the cube spatially utilizes the IFU table that lists the one-to-one correspondence between fibre positions on the IFU head and stacked spectra on the CCD (Bastian et al. 2006). A schematic representation of the data reduction processes can be found in Zanichelli et al. (2005).

Unlike other IFU designs [such as VLT Fibre Large Array Multi Element Spectrograph (FLAMES)/Argus], there are no 'sky-dedicated' fibres in VIMOS IFU mode. Sky subtraction was performed by locating a background region within each quadrant, summing the spectra over each of the spaxels in the reconstructed cube and subtracting the median sky spectrum of the region from its corresponding quadrant. Median combining was needed to ensure that any residual contamination from faint objects was removed. It should be noted that VIMOS IFU images are obtained as projections on the IFU CCD, i.e. they are mirror images to what is seen on the sky. Thus, all emission maps presented in this paper have been reflected about the *Y*-axis to obtain the correct orientation.

2.3 Emission line profile fitting

The resolving power and signal-to-noise ratio (S/N) of the data are high enough to allow the resolution of multiple components in the majority of the emission lines seen in the 1600 spectra across the FoV. In order to fit spectra of this quantity and complexity, we utilized an automated fitting procedure called PAN (Peak ANalysis; Dimeo 2005). This IDL-based, general-purpose curve-fitting package was adapted by Westmoquette et al. (2007a) for use with FITS format data by allowing multiple spectra to be read simultaneously in an array format. The user can interactively specify initial parameters of a spectral line fit (continuum level, line peak flux, centroid and width) and allow PAN to sequentially process each spectrum, fitting Gaussian profiles accordingly. The output consists of the fit parameters for the continuum and each spectral line's profile and the χ^2 value for the fit.

It was found that in the spectra of Mrk 996 most high S/N emission line profiles consist of a strong, narrow central Gaussian component (hereafter C1), superimposed on a very broad component containing a substantial proportion of the flux (hereafter C2). In addition to this, in the core of the galaxy the C2 component of the Balmer line profiles splits into two broad Gaussians of variable strength and velocity (hereafter C3 and C4, shifted towards the blue and red of the centroid of C1, respectively). The splitting of C2 into C3 and C4 and the region in which this occurs is discussed in Section 3.2. Fig. 3 shows examples of fits to the Hα emission line from different regions of Mrk 996 in order to illustrate single, double and triple Gaussian fits, along with the corresponding fit residuals. In the same figure a double Gaussian fit to the [O III] λ5007 profile is also shown corresponding to the same central spaxel for which Hα requires a triple Gaussian fit, thus illustrating the difference between the Hα and [O III] line profiles. Where appropriate, single or multiple Gaussians were fitted to the emission line profiles, restricting the minimum FWHM to be the instrumental width. Suitable wavelength limits were defined for each emission line and continuum level fit. Further constraints were applied when fitting the [S II] doublet: the wavelength difference between the two lines was taken to be equal to the redshifted laboratory value when fitting the velocity component, and their FWHMs were set equal to one another.

In order to rigorously determine the optimum number of Gaussians required to fit each observed profile the statistical *F*-test was used. The *F*-distribution function allows one to calculate the significance of a variance (χ^2) increase that is associated with a given confidence level, for a given number of degrees of freedom. We note that even though many low S/N lines may in reality be composed of multiple emission components, it is often not statistically significant to fit anything more than a single Gaussian. This is why the robust *F*-test method was chosen for objectively determining the optimum number of components to fit to each line. Resultant optimized fits for various line species are as follows.

Single narrow Gaussian (i.e. C1 component only) – [Fe III] $\lambda\lambda$4658, 4702, 4881, 4986, [O I] $\lambda\lambda$6300, 6364, [N II] λ6584, [S II] $\lambda\lambda$6717, 6731 and [O II] $\lambda\lambda$7320, 7330.

Single broad Gaussian (i.e. C2 component only) – [N II] λ5755 and [O III] λ4363.

Double narrow/broad Gaussian (C1 and C2) – all Balmer lines (excluding the central spaxels), He I $\lambda\lambda$4471, 5876, 6678, 7065, [O III] $\lambda\lambda$4959, 5007, [S III] λ6312 and [Ar III] λ7136.

Triple narrow/broad Gaussian fit (C1, C3 and C4) – all Balmer lines (central spaxels only).

The errors reported by PAN during fitting underestimate the true uncertainties. We thus follow an error estimation procedure which involves the visual re-inspection of the line profile plus fit after knowing which solution was selected by our tests, and taking into account the S/N ratio of the spectrum. The errors on the fits are minimized across the IFU's aperture varying S/N ratio during the *F*-testing procedure by selecting the number of components which best fit the profile within that particular spaxel. It is further noted that the uncertainties associated with each individual line component are coupled to those of the other components within a given line profile. By comparing PAN fits to those performed by other fitting techniques (e.g. IRAF's SPLOT task) on line profiles with an established configuration (i.e. after performing the *F*-test) we find

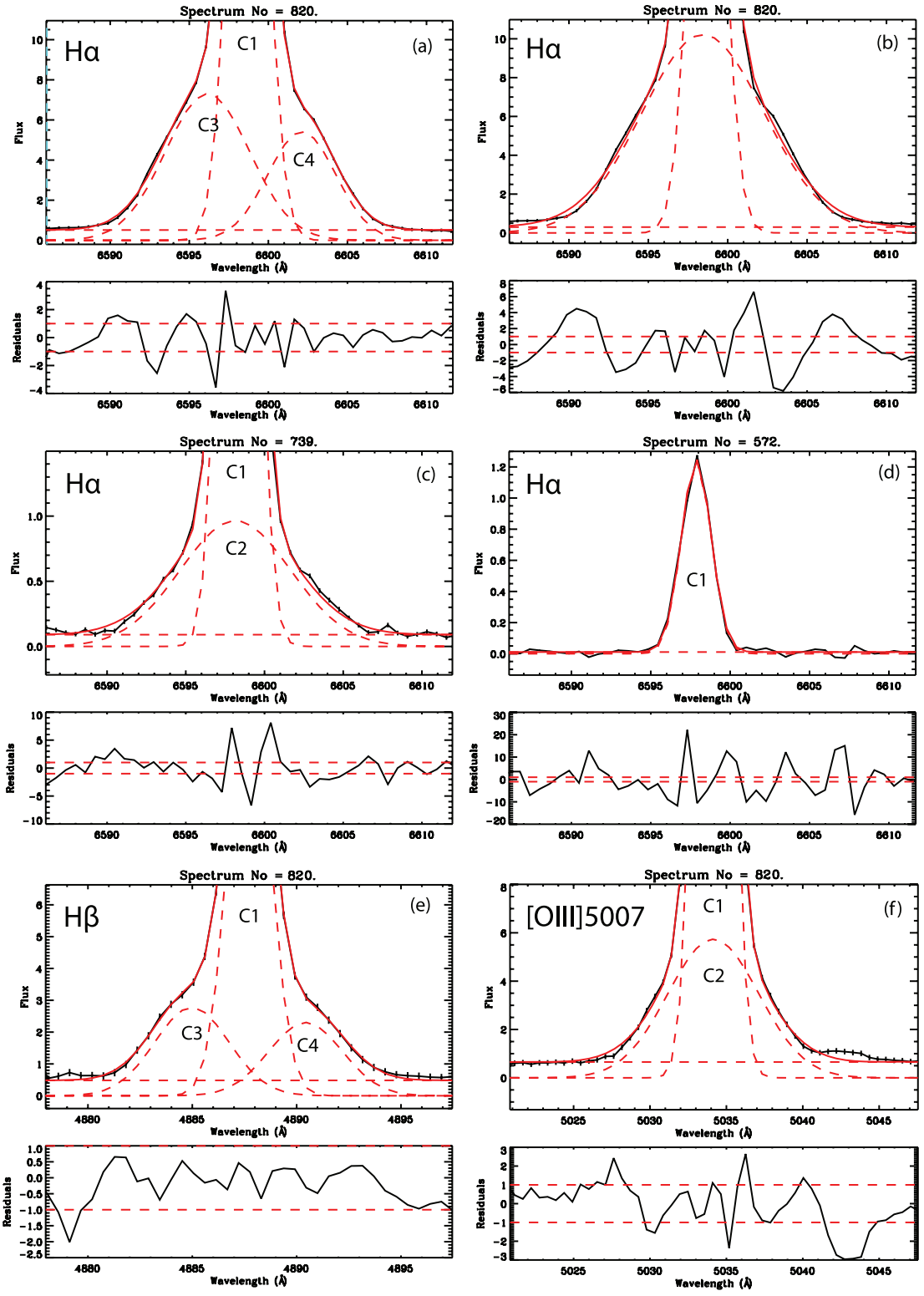

Figure 3. Example Mrk 996 emission line profiles and Gaussian fits: (a) a typical spaxel from the core region with a triple Gaussian fit to the Hα line; (b) the same spaxel spectrum shown in (a) but with a double Gaussian fit [note the larger residuals of the fit as compared to (a)]; (c) Hα emission line from a spaxel in the outer region which required a double Gaussian fit; (d) Hα emission line from the edge of the outer region where a single component fit is sufficient; (e) the Hβ emission line for the same core spaxel as that in (a), displaying the same triple component structure (Hγ also shows an identical structure in the core spaxels); (f) the [O III] λ5007 emission line for the same core spaxel as that of (a) and (b), illustrating an optimal double Gaussian fit (rather than the triple components required for the Balmer lines). The flux units are $\times 10^{-15}$ erg s^{-1} cm^{-2} Å^{-1}. The fit residuals are plotted under each panel (in units of σ) with dashed guidelines at $\pm 1\sigma$. The wavelengths are not corrected for redshift.

Table 2. Emission line measurements for summed spectra of the inner core (1.7×2.3 arcsec^2) and an 'outer annulus' region whose extent is 5.3×6.3 arcsec^2 but from which the inner core spectrum has been subtracted (see Section 3.4). Observed fluxes and dereddened intensities are given for the main two velocity components and are relative to Hβ = 100 (the corresponding velocity component of Hβ). The employed logarithmic extinction constants, c(Hβ), are quoted (see Section 3.1); integrated Hβ fluxes for the two main velocity components, in units of $\times 10^{15}$ erg cm^{-2} s^{-1}, are also listed.

		Core region			Outer region		
Line ID	Component	FWHM (km s^{-1})	$F(\lambda)$	$I(\lambda)$	FWHM (km s^{-1})	$F(\lambda)$	$I(\lambda)$
4340 Hγ	C1	145.1 ± 2.1	44.9 ± 0.5	46.3 ± 0.4	158.2 ± 6.2	54.4 ± 8.7	63.2 ± 2.2
4340 Hγ	C2	442.2 ± 15.9	42.6 ± 1.3	48.2 ± 1.4	–	–	–
4363 [O III]	C2	476.5 ± 14.4	20.2 ± 0.5	32.9 ± 0.8	–	–	–
4471 He I	C1	155.6 ± 14.8	3.8 ± 0.6	3.9 ± 0.6	260.2 ± 91.2	9.7 ± 2.9	10.8 ± 2.8
4471 He I	C2	540.6 ± 61.0	9.8 ± 1.0	10.7 ± 1.1	–	–	–
4658 [Fe III]	C1	277.5 ± 27.7	3.3 ± 0.2	3.3 ± 0.5	–	–	–
4702 [Fe III]	C1	274.3 ± 53.0	0.7 ± 0.4	0.7 ± 0.4	–	–	–
4861 Hβ	C1	130.8 ± 0.6	100.0 ± 1.0	100.0 ± 0.7	133.9 ± 0.6	100.0 ± 22.0	100.0 ± 15.6
4861 Hβ	C2	414.7 ± 4.3	100.0 ± 1.5	100.0 ± 1.0	308.5 ± 6.2	100.0 ± 21.5	100.1 ± 15.2
4881 [Fe III]	C1	313.4 ± 94.6	1.0 ± 0.4	1.0 ± 0.4	–	–	–
4959 [O III]	C1	131.2 ± 0.6	132.2 ± 1.3	131.7 ± 0.9	137.9 ± 1.75	113.1 ± 2.3	109.9 ± 2.2
4959 [O III]	C2	392.0 ± 10.3	49.3 ± 1.4	48.2 ± 1.3	332.7 ± 3.6	58.32 ± 14.8	55.4 ± 14.08
4986 [Fe III]	C1	210.5 ± 54.8	1.5 ± 0.6	1.5 ± 0.6	–	–	–
5007 [O III]	C1	132.4 ± 0.6	399.6 ± 4.2	397.1 ± 3.2	130.6 ± 0.6	347.7 ± 54.3	333.4 ± 2.5
5007 [O III]	C2	415.2 ± 13.8	148.8 ± 4.7	143.8 ± 4.3	404.4 ± 38.9	133.9 ± 24.1	124.3 ± 11.9
5755 [N II]	C2	427.9 ± 74.5	3.3 ± 0.4	4.0 ± 0.5	–	–	–
5875 He I	C1	121.5 ± 2.5	11.3 ± 0.4	10.7 ± 0.4	147.0 ± 8.7	19.6 ± 3.2	15.2 ± 0.7
5875 He I	C2	425.8 ± 8.2	33.4 ± 0.7	27.2 ± 0.5	–	–	–
6300 [O I]	C1	128.0 ± 13.8	4.6 ± 0.4	4.3 ± 0.4	141.9 ± 22.9	7.6 ± 1.5	5.4 ± 0.7
6312 [S III]	C1	107.4 ± 13.8	1.2 ± 0.2	1.2 ± 0.2	133.0 ± 31.8	3.8 ± 0.8	2.7 ± 0.4
6312 [S III]	C2	403.0 ± 29.0	5.8 ± 0.4	4.4 ± 0.3	–	–	–
6363 [O I]	C1	153.2 ± 20.3	1.7 ± 0.2	1.6 ± 0.2	147.5 ± 38.2	4.0 ± 1.1	2.9 ± 0.6
6563 Hα	C1	116.5 ± 0.9	306.9 ± 4.4	285.6 ± 3.6	118.8 ± 0.4	418.9 ± 65.3	287.6 ± 1.6
6563 Hα	C2	420.5 ± 7.3	400.5 ± 7.5	294.0 ± 4.6	407.7 ± 9.6	555.5 ± 85.3	284.2 ± 0.8
6584 [N II]	C1	126.2 ± 4.1	38.0 ± 1.1	35.3 ± 1.0	123.4 ± 2.2	45.4 ± 7.1	31.1 ± 0.4
6678 He I	C1	112.7 ± 4.9	3.5 ± 0.2	3.2 ± 0.2	124.8 ± 14.8	6.8 ± 1.3	4.6 ± 0.5
6678 He I	C2	550.3 ± 28.8	9.2 ± 0.4	6.6 ± 0.3	–	–	–
6717 [S II]	C1	118.8 ± 1.8	30.9 ± 0.5	28.6 ± 0.5	117.4 ± 2.2	31.6 ± 5.0	21.2 ± 0.4
6731 [S II]	C1	118.5 ± 1.8	24.6 ± 0.5	22.8 ± 0.4	117.2 ± 2.2	22.4 ± 3.5	14.9 ± 0.4
7065 He I	C1	76.00 ± 65.4	1.1 ± 0.9	1.0 ± 0.8	217.8 ± 56.1	7.0 ± 1.9	4.4 ± 1.0
7065 He I	C2	425.4 ± 58.2	24.4 ± 2.8	16.8 ± 1.9	–	–	–
7136 [Ar III]	C1	127.3 ± 17.2	10.3 ± 2.3	9.4 ± 2.1	127.8 ± 11.4	13.5 ± 2.3	8.5 ± 0.7
7136 [Ar III]	C2	441.0 ± 213.9	8.2 ± 3.5	5.6 ± 2.4	–	–	–
7320 [O II]	C1	176.6 ± 11.9	6.1 ± 0.3	5.6 ± 0.3	219.2 ± 62.3	9.2 ± 2.3	5.6 ± 1.1
7330 [O II]	C1	165.3 ± 11.9	5.8 ± 0.3	5.3 ± 0.3	111.3 ± 21.3	10.8 ± 2.2	6.6 ± 0.8
c(Hβ)	C1		0.10 ± 0.02			0.51 ± 0.08	
c(Hβ)	C2		0.42 ± 0.04			0.91 ± 0.12	
F(Hβ)	C1		626.30 ± 4.31			180.33 ± 28.13	
F(Hβ)	C2		431.70 ± 4.46			36.67 ± 5.57	

that uncertainties of ∼5–10 and ∼15–20 per cent are associated with the C1 and C2–C4 fits, respectively. A listing of measured flux and FWHM uncertainties appears in Table 2, where errors are quoted for individual component fits to emission lines detected on integrated spectra across the inner and outer regions of Mrk 996.

2.4 Cube alignment and correction for differential atmospheric refraction

Observations of an object's spectrum through the Earth's atmosphere are subject to refraction as a function of wavelength, known as differential atmospheric refraction (DAR). The direction of DAR is along the parallactic angle at which the observation is made. Each reduced data cube was corrected for this effect using the algorithm outlined by Walsh & Roy (1990); this procedure calculates fractional pixel shifts for each monochromatic slice of the cube relative to a fiducial wavelength (i.e. a strong emission line), shifts each slice with respect to the orientation of the slit on the sky and the parallactic angle and recombines the DAR-corrected data cube. Having data cubes with different wavelength ranges would ideally involve a choice of fiducial wavelength that is common to both, e.g. He I λ5876 for these VIMOS data. However, the S/N ratio of this line is not consistently high across the IFU aperture, and pixel shifts for each cube relative to this line were found to be unreliable. Instead, we chose to correct each data cube using its strongest emission line: Hβ for the HRblue cube and Hα for the HRorange cube. The two cubes were then spatially matched by aligning the Hα and Hβ emission contours using a 2D Gaussian fit. This involved a maximum shift of -0.73 spaxels in X and $+0.82$ spaxels in Y. Two effects can introduce minor errors when aligning monochromatic H I images: (i) an extinction gradient across the observed region disproportionately affecting the two lines, and (ii) the presence of a temperature

gradient, since the H I lines have a very slightly different temperature dependence. However, both gradients would need to be significant for substantial errors to be introduced; the subspaxel shifts that were determined show that this is not the case here.

3 MAPPING OF LINE FLUXES AND KINEMATICS

3.1 Line fluxes and reddening correction

Full HRblue and HRorange spectra are shown in Fig. 2, with identified emission lines labelled. Table 2 lists the measured FWHM and observed and dereddened fluxes for the main velocity components of the detected emission lines. The fluxes are from spectra summed over the core region and the outer annulus region, as defined in Section 3.4, and are quoted relative to the flux of the corresponding Hβ component. They were corrected for reddening using the Galactic reddening law of Howarth (1983) using c(Hβ) values derived from the Hα/Hβ and Hγ/Hβ line ratios of their corresponding components, weighted in a 3:1 ratio, respectively, in conjunction with the theoretical Case B ratios from Hummer & Storey (1987). Following the same method, an average c(Hβ) map was also derived using ratioed Hα/Hβ and Hγ/Hβ emission line maps. The c(Hβ) map was used for correcting emission line maps for reddening in order to then create abundance maps. In the direction to Mrk 996 a foreground Milky Way reddening of $E(B-V) = 0.04$, corresponding to c(Hβ) = 0.06, is indicated by the extinction maps of Schlegel, Finkbeiner & Davis (1998). Values of c(Hβ) of 0.10 ± 0.02 and 0.51 ± 0.08 are applicable to the narrow component emission in the inner and outer regions of Mrk 996, respectively, while values of 0.42 ± 0.04 and 0.91 ± 0.12 are applicable to the broad component emission for the inner and outer regions, respectively.

3.2 The Balmer line properties

All the Balmer lines detected from Mrk 996 (Hα, Hβ and Hγ) show a common multicomponent velocity structure which in the innermost spaxels is exclusive to the Balmer lines, i.e. it is not seen in the forbidden lines. Here we present a discussion of the highest S/N ratio H I line, Hα. Maps of the individual Hα velocity components (flux, radial velocity and FWHM) are shown in Fig. 4. As mentioned previously, up to three components are resolved in the Hα line profile in the nuclear region of Mrk 996.

(i) A central, narrow Gaussian (C1) is detected throughout the galaxy (see the flux map in Fig. 4a), peaking at $\alpha = 01^{\rm h}27^{\rm m}35\overset{\rm s}{.}5 \pm 0.1$, $\delta = -06^\circ 19' 36\overset{''}{.}2 \pm 0.2$ (J2000), with a surface brightness of 10.1×10^{-12} erg cm^{-2} s^{-1} arcsec^{-2} in the central region, and gradually decreasing over a region with a major axis radius of 3.84 arcsec (403 pc) and a minor axis of 2.39 arcsec (251 pc); beyond this the Hα emission traces a very low surface brightness area (which TIL96 fitted with an exponential disc on their *HST* images). The galaxy does not show a smooth elliptical shape when viewed in Hα. Fig. 1 shows the flux contours of the narrow Hα component (C1) overlaid on the *HST* F569W (V-band) image. The Hα emitting region imaged by VIMOS is mostly confined within the inner part of the F569W image but the major axes of the two are not aligned. A dust extinction feature is present in the north-west section of the inner star-forming region that distorts the F569W flux isophotes (TIL96). The dust feature also distorts the outermost Hα contours of the VIMOS data.

(ii) In the very core of Mrk 996, over an area of $\sim$1.5 arcsec in radius (162 pc), the narrow C1 profiles are accompanied by broad underlying components that are best fit with two Gaussians (C3 and C4) to the blue and red of C1, respectively (Fig. 4a). The significance of these features is discussed below.

(iii) Beyond a radius of $\sim$1.5 arcsec from the core, C3 and C4 blend into a single broad Gaussian (C2) (Fig. 4a). The region over which this component is seen is $\sim$2–4 arcsec in radius (216–432 pc); its outer boundary matches well that of the brightest portion of the C1 flux map.

The radial velocity map of component C1 (Fig. 4b) shows a strong velocity gradient from west to east, with a definable axis of rotation at PA = 5° (marked by the dashed line across the C1 velocity map). Neither the rotation axis as revealed by VIMOS nor the axis normal to it is aligned with the apparent, i.e. photometric, major axis of the galaxy which lies at PA $\sim$ 23° (TIL96). A velocity gradient in approximately the same direction is observed in the broad component C2, although in this case the negative velocity component is not exactly balanced by a positive counterpart. Fig. 5 shows position–velocity (P–V) diagrams along the adopted axis of rotation (Fig. 5a) and also perpendicular to this axis (Fig. 5b). A new estimation of the heliocentric systemic velocity of Mrk 996 can be made using Fig. 5(a); a radial velocity of 1642 ± 10 km s^{-1} is needed to normalize the distribution of C1 velocities along the axis of rotation to zero (cf. the 1622 ± 10 km s^{-1} estimate of TIL96). The narrow line component C1 shows a velocity gradient along the direction normal to the rotation axis, with radial velocities ranging from ~ -50 to $+50$ km s^{-1}, and the P–V diagram of component C1 shows a linear velocity gradient indicating solid-body rotation (Fig. 5b). This type of structure is not uncommon for BCDs observed in the H I 21-cm line and has been used by van Zee, Salzer & Skillman (2001) to constrain evolutionary scenarios. Assuming a Keplerian velocity profile we have converted each radial velocity data point of component C1 (Fig. 5b) into a mass within radius r, as shown in Fig. 6. This plot shows dynamical mass growing at similar rates on either side of the centre, rising to a total mass of $\sim 5 \pm 1 \times 10^8$ M$_\odot$ within a radius of $\sim$0.75 kpc. This is in good agreement with the total mass of 4.3×10^8 M$_\odot$ estimated by TIL96 from H I emission features detected by Thuan, Izotov & Lipovetsky (1995). It should be noted that all previous kinematical studies of BCDs have been based on H I 21-cm observations (van Zee et al. 2001; Thuan, Hibbard & Lévrier 2004). The broad line component C2 also shows a velocity gradient roughly perpendicular to the rotation axis (Fig. 5b), aligned more closely with the major axis of Mrk 996, with radial velocities that merge with those of C1 2 arcsec from the centre of the galaxy, but extending to larger negative values. No definite velocity structure can be seen along this axis for the C3 and C4 components; however, these show an opposing velocity gradient along the galaxy's rotation axis (Fig. 5a). Their radial velocities lie much higher at -60 to -160 km s^{-1} for C3 and $+110$ to $+210$ km s^{-1} for C4, with the gradients in both showing a similar 'S' shape offset by 1 arcsec from the dynamical centre of Mrk 996. It is further noted that the velocity centre of symmetry of the 'S' feature is offset by $+50$ km s^{-1} from the heliocentric systemic velocity of Mrk 996 measured above. The 'S' kinematic feature can be attributed to a two-arm spiral structure located at the nucleus of Mrk 996, whose approaching and receding arms are, respectively, traced by the velocity distribution of the C3 and C4 components of Hα. Furthermore, our analysis reveals that the projected angular velocity vectors on the plane of the sky of the spiral and of the gas traced by the C1 narrow line component are at an angle of $< 90^\circ$. In their WFPC2 images of Mrk 996, TIL96

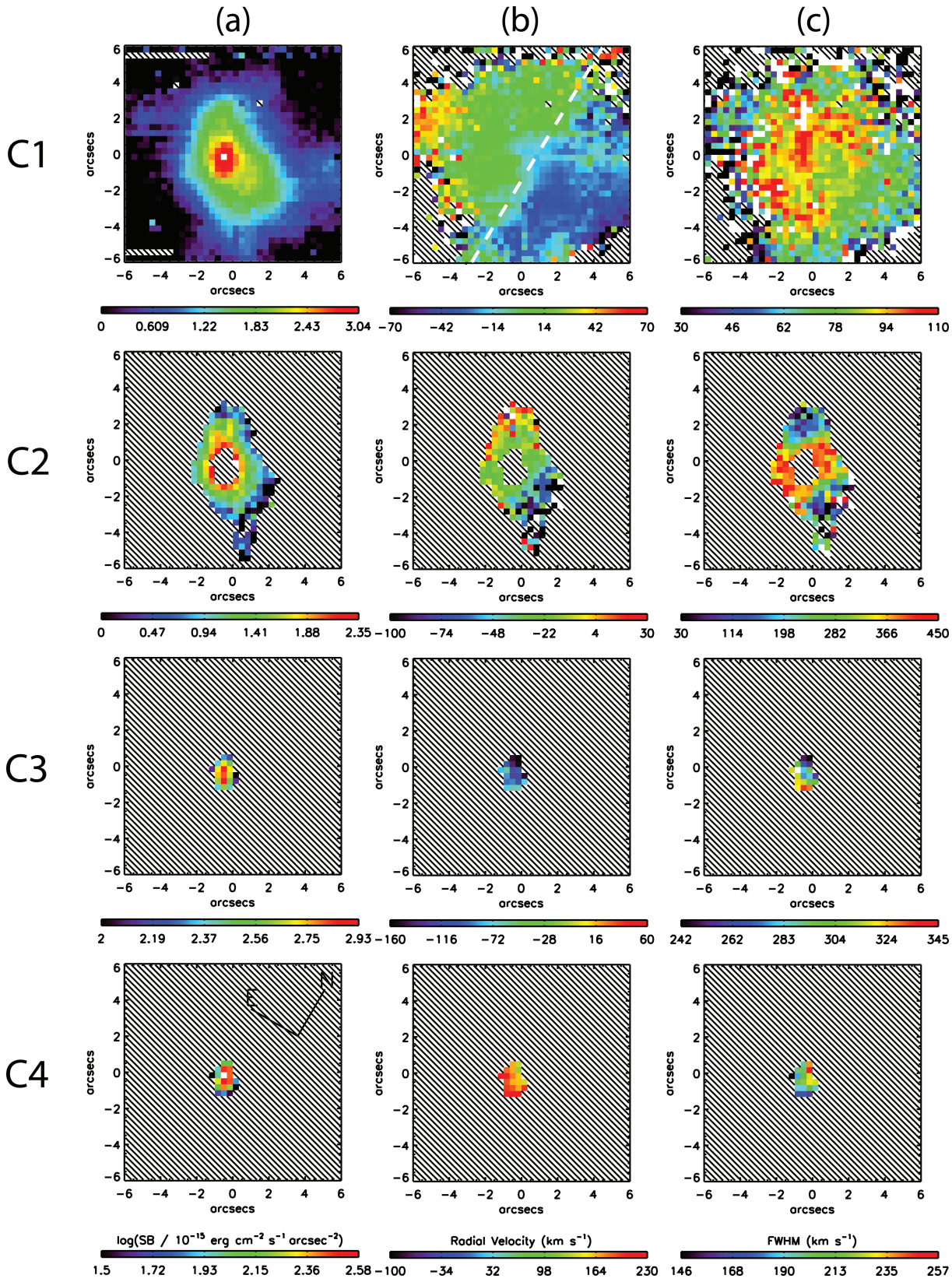

Figure 4. Maps of Mrk 996 in the Hα velocity components C1–C4; (a) logarithmic surface brightness; (b) radial velocity (relative to the heliocentric systemic velocity of +1642 km s^{-1}), where the white dotted line overlaid on the C1 velocity map represents a cut along the rotational axis, as used for the P–V diagrams shown in Fig. 5; (c) FWHM corrected for the instrumental PSF. See text for details.

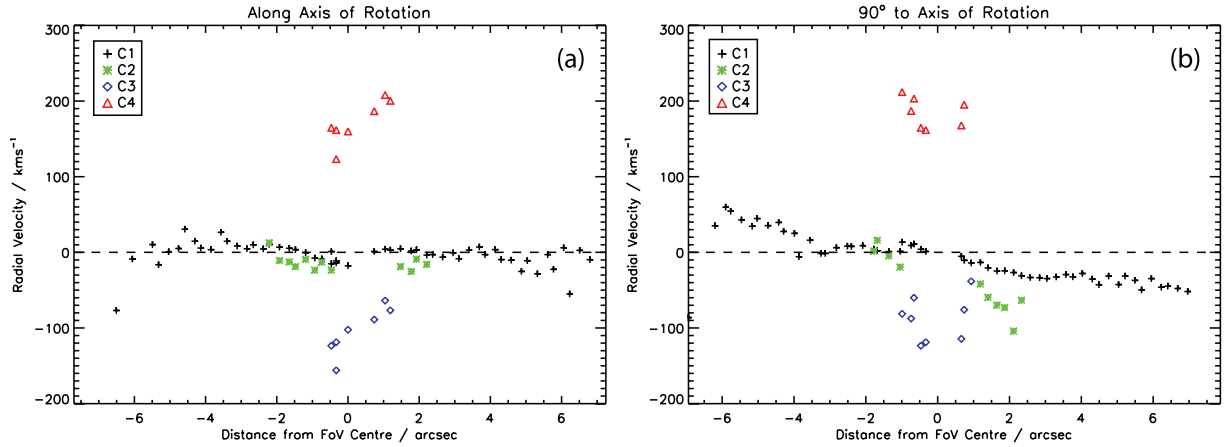

Figure 5. P–V diagrams for Hα: (a) along the axis of rotation, defined as 5° east of north, as indicated by component C1 in Fig. 4(b); (b) along the direction 90° to the rotation axis. Both diagrams are relative to a systemic velocity of +1642 km s^{-1}. Typical radial velocity errors are <3, 8–20, 12–15 and 7–11 per cent for C1, C2, C3 and C4, respectively, with a spatial error of 0.5 spaxels (±0.17 arcsec).

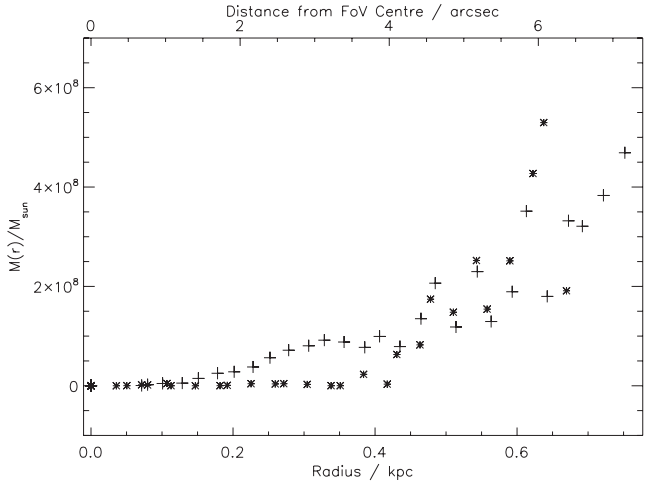

Figure 6. Dynamical mass as a function of radius, *r*, derived from the distribution of C1 radial velocities along the direction normal to Mrk 996's rotation axis: distance east from the centre represented by crosses and distance west from the centre represented by stars.

identified a small spiral structure along the east–west direction (see their fig. 4b) whose pivot is the nuclear star-forming region which is slightly offset from the centre of the outermost F791W image isophotes. The pivot of the spiral and the peak flux position on the VIMOS Hα C1 map coincide spatially. The 1 arcsec offset mentioned above for the spatial centre of symmetry of the 'S' feature (Fig. 5a) is consistent with the asymmetry noted by TIL96. This fact, along with the $\sim +50$ km s^{-1} offset of the spiral's pivot with respect to the systemic velocity of the galaxy, indicates that the spiral-like nucleus of Mrk 996 is kinematically decoupled to some degree from the main ionized gas component. This could indeed be the fossil kinematic signature of a past merger event.

The FWHMs of C1–C4 in Hα are shown in Fig. 4(c), corrected for the instrumental point spread function (PSF; see Section 2.2). A peak in the FWHM of the narrow C1 component, $\sim$110 km s^{-1}, is seen at the nucleus of Mrk 996. This gradually, but not uniformly, decreases to $\sim$65 km s^{-1} towards the outer regions. The gradient in the FWHM of C2 is far stronger, peaking at $\sim$450 km s^{-1} at two positions north-west and south-east of the nucleus and decreasing to $\sim$100 km s^{-1} elsewhere: the broader linewidths along the former direction could be the signature of an expanding shell surrounding the inner star-forming region, blown outwards by the stellar winds of the core cluster. Higher resolving power IFU spectroscopy is needed to disentangle the kinematics of this region. No significant gradient is seen in the FWHM of components C3 and C4, both remaining between 200 and 300 km s^{-1}.

3.3 The [O III] nebular line properties

As mentioned previously, the structure of the H I Balmer lines is not mirrored in the forbidden nebular lines. All the strong forbidden lines (with the exception of [O III] λ4363 and [N II] λ5755 discussed below) are composed of a narrow, central Gaussian (C1) with an underlying *single* broad Gaussian component (C2). An optimal fit, after applying the rigorous statistical *F*-test to a spaxel from the core of Mrk 996, can be seen in Fig. 3(f). For the spaxels in which the Balmer components C3 and C4 are detected, the FWHM of the [O III] λ5007 C2 component is $\sim$390–415 km s^{-1} and that of each of Hα C3 and C4 is $\sim$180–240 km s^{-1}. The occurrence of additional C3–C4 components in the Balmer lines is in contrast to the non-occurrence of C2 splitting in the [O III] nebular lines and can perhaps be ascribed to a lower S/N ratio for the broad component of [O III] $\lambda\lambda$4959, 5007 compared to the C2 of H I lines: the observed C2/C1 flux ratios pertaining to the [O III] nebular lines in the inner core of Mrk 996 (as defined in the following subsection) are half of those observed in the H I lines (Table 2). However, from our analysis of the broad C2 component, we find $\log(N_e/\mathrm{cm}^{-3}) = 7.25 \pm 0.25$ from the [O III] lines (Section 4). This is high enough to collisionally suppress $\lambda\lambda$5007+4959 whose critical density for de-excitation is 6.4×10^5 cm^{-3}. The distribution of flux in the C1 and C2 components of the [O III] λ5007 line is shown in Fig. 7. The shape and extent of the emitting regions are similar to those of the corresponding Hα C1 and C2 components.

3.4 Broad emission lines: [O III] λ4363 and [N II] λ5755

Our multicomponent line analysis shows that only the broad (C2) components of the auroral [O III] λ4363 and [N II] λ5755 transitions are present, and only in the inner galaxy. The implications of this for the use of [O III] λ4363 as a temperature diagnostic are discussed in Section 4. For the purpose of this study the λ4363 spectral map (Fig. 8) is used to define a two-region model of Mrk 996: an 'inner

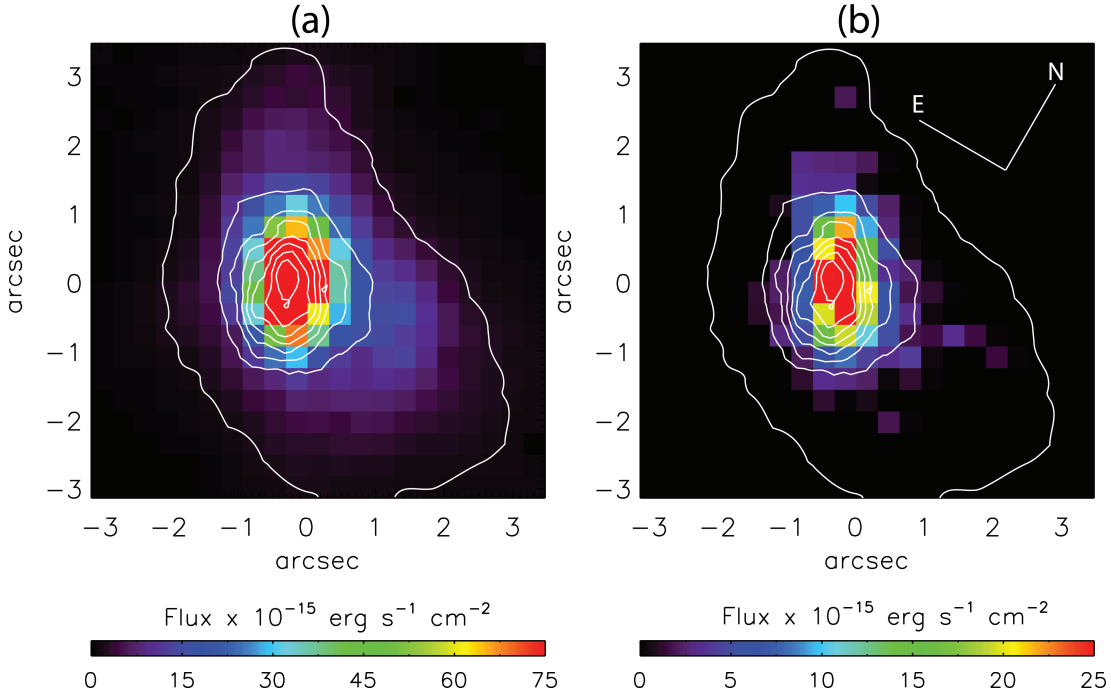

Figure 7. [O III] λ5007 emission line maps of Mrk 996 showing the flux distribution per 0.33 × 0.33 arcsec^2 spaxel: (a) in the narrow C1 component; (b) in the broad C2 component. Overlaid are the Hα narrow component contours (white), as shown in Fig. 1.

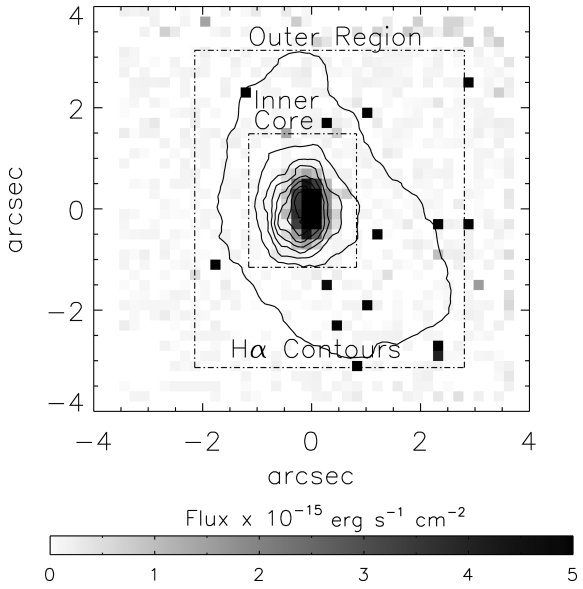

Figure 8. Flux distribution of [O III] λ4363 per 0.33 × 0.33 arcsec^2 spaxel with Hα contours overlaid. The area over which λ4363 is detected is used to define an 'inner core' region, with a surrounding 'outer region' covering the full extent of the Hα emission.

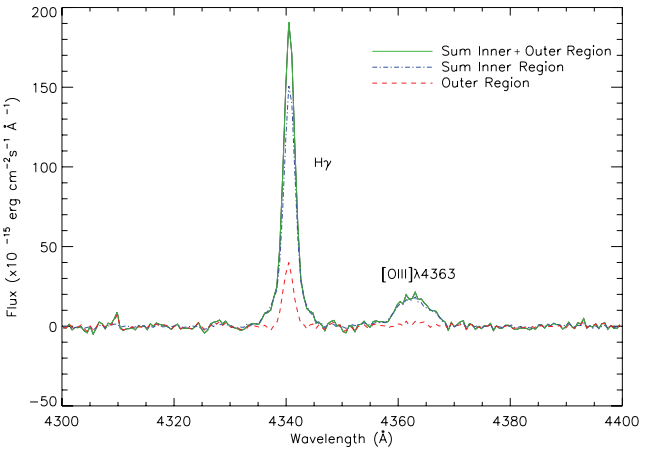

Figure 9. Summed spectra from the inner core and the outer region illustrating the lack of detectable [O III] λ4363 in the outer region of Mrk 996.

core' region, defined by λ4363 emission extending over an area of 1.7 × 2.3 arcsec^2 (185 × 250 pc^2), and an 'outer region' large enough to incorporate almost the full extent of Hα emission over an area of 5.3 × 6.3 arcsec^2 (575 × 685 pc^2). The lack of any detectable [O III] λ4363 emission in the outer region is illustrated in Fig. 9. Here we compare the summed spectrum of the outer region plus core with the summed spectrum of the core region, and also show the residual outer region spectrum. An emission line map of the broad [N II] λ5755 line is shown in Fig. 10(a); its flux distribution correlates strongly with that of the similarly broad λ4363, suggesting that the excitation of these lines is affected by processes that are particular to the inner core region of Mrk 996. In Fig. 11 the velocity profiles of the broad C2 components of Hα, Hβ and [O III] λ5007 are shown, overlaid in velocity space with the profiles of the [O III] λ4363 and [N II] λ5755. Each spectral line has been summed over the inner core region and all show a FWHM of ∼300 km s^{-1}, suggesting that a common excitation mechanism is responsible for the emission of the broad component. The larger widths of [O III] λ4363 and [N II] λ5755 indicate that the physical conditions within the inner core are different from those in the outer region.

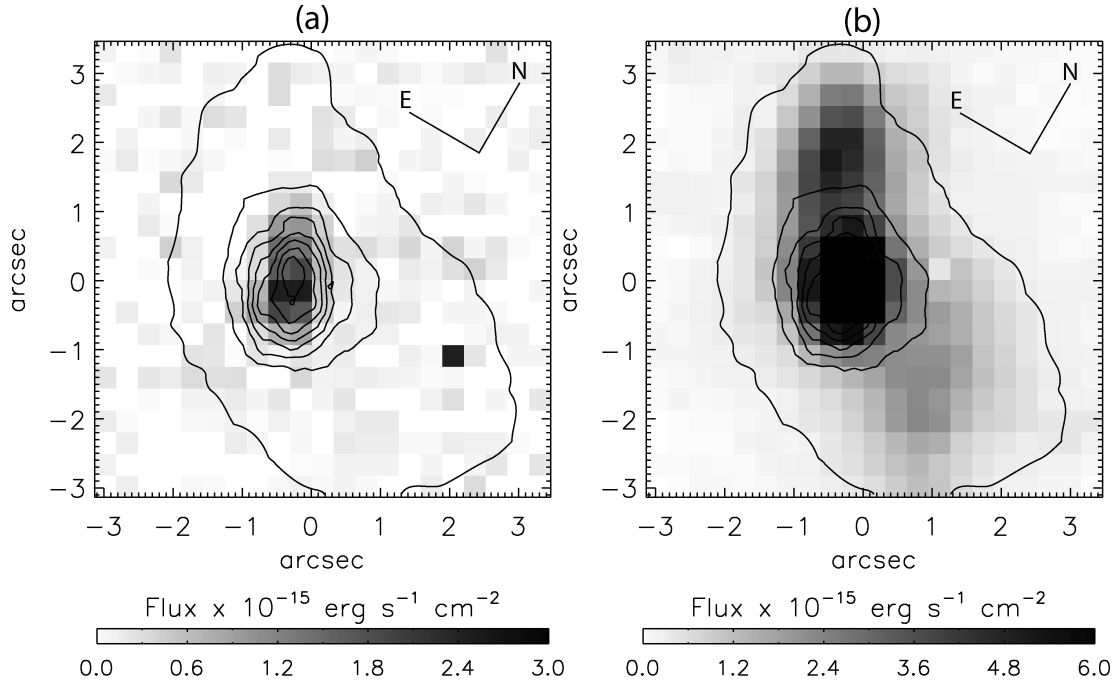

Figure 10. Flux distribution per 0.33 × 0.33 arcsec^2 spaxel of (a) [N II] λ5755 for which only a broad component is detected and which is seen only within the core region; (b) [N II] λ6584, whose flux distribution peaks in the core and towards the north-east; a fainter peak is seen west of the core. Overlaid are the Hα narrow component contours as shown in Fig. 1.

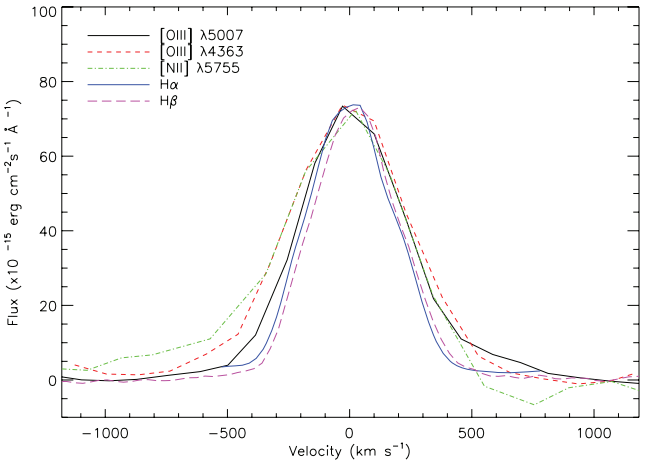

Figure 11. Velocity profiles of the broad C2 components of Hα, Hβ, [O III] λ5007 and of [O III] λ4363, [N II] λ5755 emission lines (relative to the heliocentric systemic velocity of +1642 km s^{-1}). Spectra have been summed over the inner core 1.7 × 2.3 arcsec^2 region of Mrk 996.

4 MULTICOMPONENT DIAGNOSES: ELECTRON TEMPERATURE AND DENSITY

The multicomponent nature of the emission lines from Mrk 996 must be taken into account when applying plasma diagnostic methods. For example, since [O III] λ4363 is only detected from the central region of Mrk 996 and completely lacks the narrow line component that [O III] λλ4959, 5007 exhibit (see Fig. 9), an integrated [O III] (λ5007+λ4959)/λ4363 ratio cannot provide a useful temperature diagnostic; this would lead to incorrect results. Previous analyses lacked the spectral and spatial resolution needed to decompose the line profiles and were forced to assume a single density of $N_e \sim 10^6$ cm^{-3} in order to match the anomalously low integrated [O III] (λ5007+λ4959)/λ4363 flux ratio (TIL96).

The detection of separate narrow and broad line components opens up the possibility of determining separate electron temperatures and densities and conducting a separate abundance analysis for each.

4.1 The narrow component gas

In order to estimate the electron temperature (T_e) from which the narrow line component C1 emission arises the following method was used. An upper limit to the T_e applicable to the H I and [O III] nebular C1 components can be obtained via the simulation of a narrow [O III] λ4363 component using the observed narrow λ5007 component. Predicted λ4363 C1 line intensities were obtained by multiplying the observed λ5007 C1 profile by the theoretical λ4363/λ5007 intensity ratio for a range of T_e's at $N_e = 170$ cm^{-3}; the latter was measured from the [S II] doublet ratio as described below. It should be noted that the [S II] lines only show narrow C1 components (Table 2). The scaling factors were applied to both the inner core and outer region C1 component λ5007 absolute fluxes. Simulated narrow λ4363 profiles of decreasing intensity were then subtracted from the observed λ4363 line until the residual was no longer detectable, as shown for the core region λ4363 profile in Fig. 12. It is found that a measurable narrow λ4363 C1 component would be detectable at an electron temperature of >10 000 K for both the inner core and the outer region. Thus we adopt an upper limit of 10 000 K to the electron temperature of the gas emitting the C1 component throughout Mrk 996. In Section 5.2 we argue that this limit is closer to 9200 K, based on the inference that these O/H abundance ratio across the narrow and broad line emitting regions is invariant.

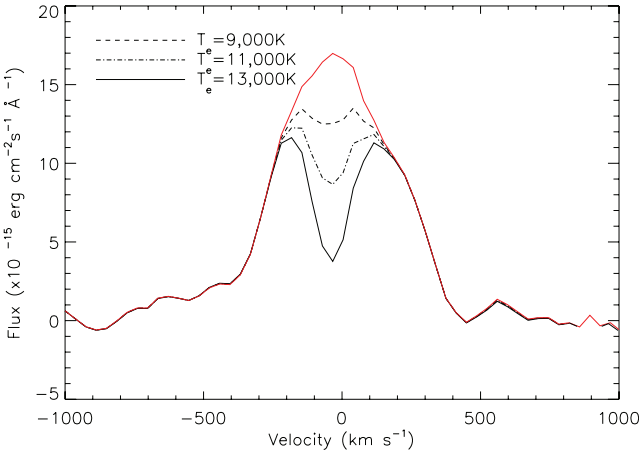

Figure 12. Inner core region dereddened [O III] λ4363 profile (solid red curve) with simulated narrow components subtracted from it, corresponding to the dereddened [O III] λ5007 narrow component profile, normalized to the different λ4363 flux levels that correspond to different adopted T_e values. The subtracted narrow component profiles correspond to electron temperatures of 9000, 11 000 and 13 000 K for an electron density of 170 cm^{-3}. An upper limit of 10 000 K is estimated for the T_e of the gas emitting the narrow C1 component in the inner core region. See text for details.

Table 3. Electron densities derived from the narrow line [S II] λ6716/λ6731 intensity ratios (1.26 ± 0.03 and 1.41 ± 0.03, respectively, for the inner core and outer region of Mrk 996).

Adopted T_e (K)	N_e (cm^{-3}) core region	N_e (cm^{-3}) outer region
9 000	170 ± 40	10^{+30}_{-9}
11 000	170 ± 40	10^{+30}_{-9}
13 000	170 ± 40	10^{+30}_{-9}

The [S II] λλ6717, 6731 lines, whose intensity ratio is a common electron density diagnostic for H II regions, show only the narrow emission component and were used to compute density values for a range of electron temperatures for the inner and outer regions of the galaxy (Table 3, using the IRAF's[2] TEMDEN task of the NEBULA package). These densities are representative of conditions in the gas from which the narrow component emission arises. This propels us to use alternative methods to investigate the density of the gas emitting the broad line components in the inner core region of Mrk 996. With the electron temperature of $T_e \leq 10\,000$ K obtained above, we find that electron densities of 170 and 10 cm^{-3} are representative of the narrow C1 component gas in the inner and outer regions of Mrk 996, respectively.

4.2 [Fe III] line diagnostics

[Fe III] emission line ratios provide useful density diagnostics that can trace both high and low electron densities; see Keenan et al. (2001). The summed spectrum of Mrk 996 (Fig. 2) shows a few of the brightest transitions among the 3d^6 levels of Fe III; [Fe III] λλ4658, 4702, 4881, 4986 and 5270. The flux in these lines above the continuum level was measured by integrating over the line profile. To maximize accuracy, the fluxes for λ4658 and λ4702 were measured after removing any contamination from WR stellar features by subtracting the WR template fit derived in Section 6. Fig. 13 shows the extinction corrected fluxes of λ4881 and λ5270 relative to λ4658 along with theoretical ratios as a function of N_e, for T_e's between 7000 and 20 000 K, from Keenan et al. (2001). Interpolating between the theoretical data for an adopted T_e of 10 000 K, the λ4881/λ4658 ratio indicates $\log(N_e/\mathrm{cm}^{-3}) = 5.7 \pm 0.3$, which falls within the somewhat larger range of $\log(N_e/\mathrm{cm}^{-3}) = 6.5^{+0.5}_{-1.5}$ implied by the observed λ5270/λ4658 ratio. These results indicate the presence of a very dense ionized medium throughout the inner core of Mrk 996.

In contrast to the above, however, the [Fe III] λ4986/λ4658 ratio is a more sensitive tracer of low electron densities. Fig. 14 shows that relative to λ4658 the λ4986 line should not be detectable at densities higher than ∼1000 cm^{-3}; the fact that the line is detected from Mrk 996 indicates the presence of a low-density gas component as

[2] IRAF is distributed by the National Optical Astronomy Observatory, which is operated by the Association of Universities for Research in Astronomy.

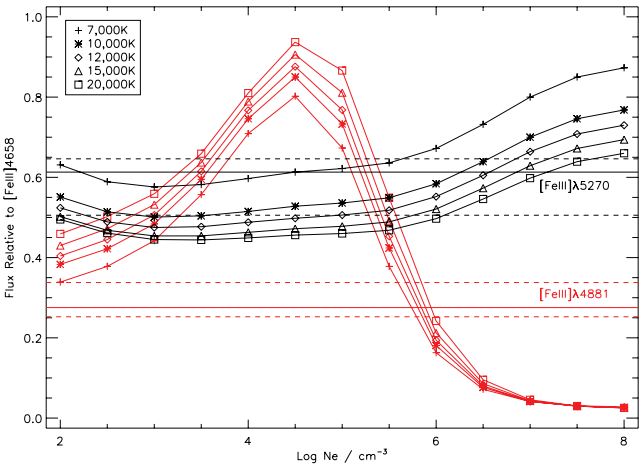

Figure 13. Theoretical [Fe III] line flux ratios, for λ4881 (red) and λ5270 (black), relative to λ4658 as a function of electron density for temperatures between 7000 and 20 000 K. The horizontal lines denote the observed flux ratios (solid) and their uncertainties (dashed) from the summed spectra of the inner core region of Mrk 996.

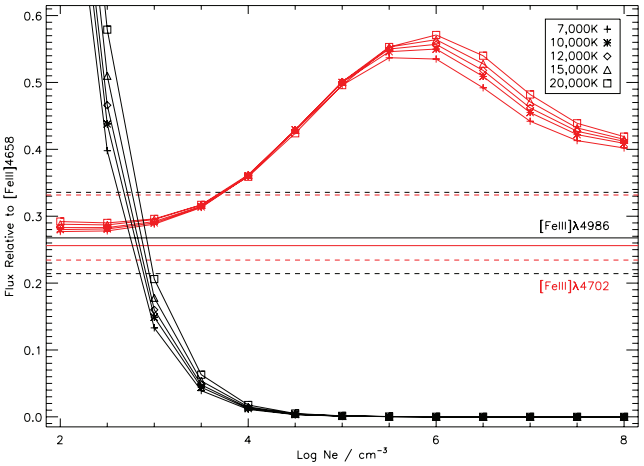

Figure 14. Theoretical [Fe III] line flux ratios, for λ4986 (black) and λ4702 (red), relative to λ4658 (in the region in which λ4986 is seen) as a function of electron density for temperatures between 7000 and 20 000 K. The horizontal lines denote the observed flux ratios (solid) and their uncertainties (dashed) from the summed spectra of the region where λ4986 is detected.

well. This is not inconsistent with the high densities derived above for the inner core as the spatial distribution of λ4986 emission (not shown) contrasts strongly with that of the other [Fe III] lines – rather than peaking in the core of the galaxy, λ4986 is distributed throughout Mrk 996 and is not confined to the inner region defined by the broad [O III] λ4363 emission. There is a clear detection of λ4986 emission over a group of 8 spaxels extending ∼1.6 arcsec east from the core. The λ4986/λ4658 and λ4702/λ4658 intensity ratios integrated over these 8 spaxels (Fig. 14) confirm that this is a low-density area ($N_e \sim 100$–$1000\,cm^{-3}$), typical of normal H II regions. This emission could be tracing lower density ionized gas throughout Mrk 996. In a study of high excitation nebulae in the Magellanic Clouds by Nazé et al. (2003), [Fe III] λ4986 was only detected in the shell of the superbubble surrounding the bright Hα nebula N44C. Because of the large distance of Mrk 996, we are unable to resolve any bubbles surrounding the central superstar cluster even though their presence in the galaxy is likely.

4.3 The broad component gas

The [O III] (λ5007+λ4959)/λ4363 intensity ratio can be used to determine the electron temperature of the gas from which the broad component emission arises. Since, however, [O III] λ4363 is only detected as a broad line, this dictates that T_e estimates using [O III] can only involve the broad C2 components; moreover, these will only be applicable to the inner core region of the galaxy where λ4363 is detected. The FWHMs of components C2 in λλ4959, 5007 are very similar to that of λ4363, all being in the range of 320–515 km s^{-1} across the inner core region; their surface brightness distributions are also similar. Furthermore, in support of the suitability of the [O III] ratio involving the C2 components is that we do not find any indication of C3 or C4 components in the highest S/N ratio emission line profiles of λλ4959, 5007 (see Fig. 3(f) for an optimized two-component fit to the λ5007 emission line from the inner core region). Even so, electron temperatures derived using only the broad line components are unphysically high (>30 000 K) until densities higher than $N_e = 10^6\,cm^{-3}$ are adopted.

We can attempt to constrain the electron temperature and density of the broad line component by using the λ1663/λ4363 and λ5007/λ4363 intensity ratios, which due to their considerably different O^{2+} upper level excitation energies can act as sensitive temperature and density diagnostics between the critical densities of each of these lines. The FOS UV spectra presented by TIL96 revealed a weak O III] λ1663 line detection which, due to its high excitation energy, ought to originate from the same gas emitting the broad [O III] λ4363 that we detect. Using a simulated FOS aperture on our broad component flux maps for λ5007 and λ4363, fluxes of $39.6 \pm 6.3 \times 10^{-15}$ erg cm^{-2} s^{-1} for λ4363 and $214.1 \pm 14.2 \times 10^{-15}$ erg cm^{-2} s^{-1} for λ5007 are predicted to fall within the small FOS aperture centred on the nucleus of Mrk 996. Together with the λ1663 flux of $1.9^{+0.4}_{-0.2} \times 10^{-15}$ erg cm^{-2} s^{-1} measured from the FOS spectrum, these fluxes were then dereddened using an average $c(H\beta)$ of 0.65 for a simulated FOS aperture on the broad component VIMOS $c(H\beta)$ map, to yield λ4363/λ1663 and λ5007/λ4363 intensity ratios of 2.4 and 4.3, respectively. The theoretical λ4363/λ1663 and λ5007/λ4363 ratios for $\log(N_e/cm^{-3}) = 5.0$–10.0 and $T_e = 5000$–30 000 K are presented in Figs 15(a) and (b) and the resultant set of solutions are shown in Fig. 15(c). The two curves in Fig. 15(c)

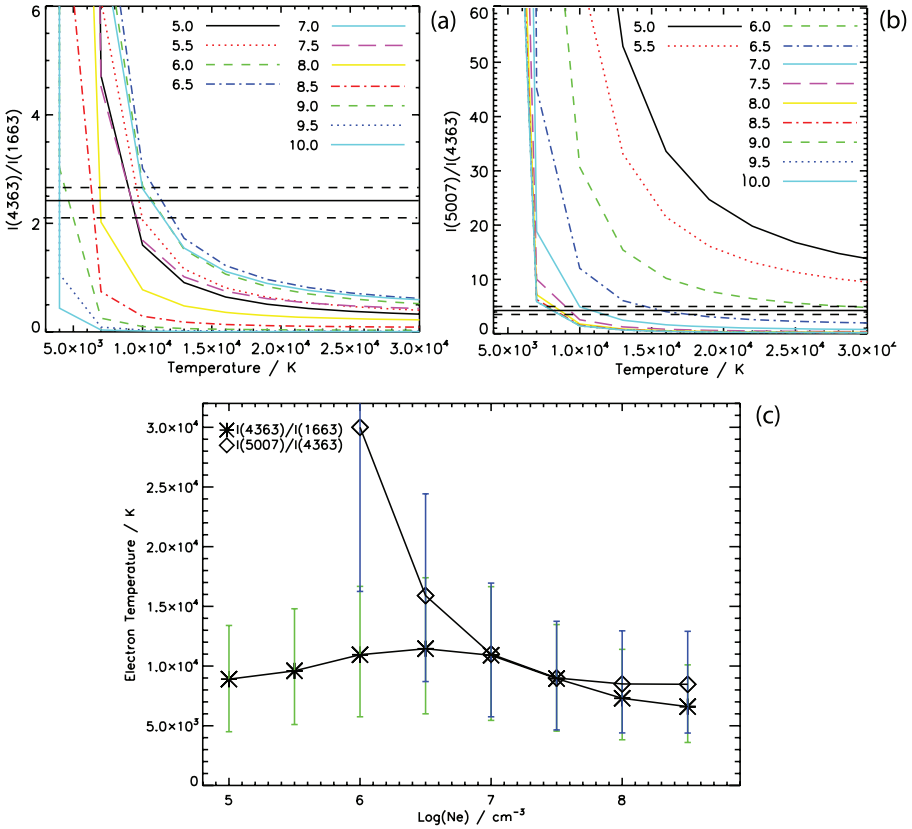

Figure 15. Broad component T_e and N_e diagnostic diagrams for (a) $I(\lambda4363)/I(\lambda1663)$ and (b) $I(\lambda5007)/I(\lambda4363)$, showing theoretical ratios for $T_e = 5000$–30 000 K and $\log(N_e/cm^{-3}) = 5.0$–10.0. The horizontal solid lines in (a) and (b) denote the observed dereddened ratios and their uncertainties (dashed); (c) shows the (T_e, N_e) solutions applicable to Mrk 996 obtained from (a) and (b) and their uncertainties.

overlap between log (N_e/cm^{-3}) = 6.5–8.5 and T_e = 7000–14 000 K. We thus adopt $T_e = 10\,500 \pm 3500$ K and $\log(N_e/cm^{-3}) = 7.25^{+1.25}_{-0.75}$ for the broad component emitting gas. The inferred density range is somewhat higher than the value derived from the [Fe III] λ4881/λ4658 ratio (Section 4.2) and supports the conclusion that the central regions of Mrk 996 contain very dense zones of ionized gas.

5 CHEMICAL ABUNDANCES

5.1 Narrow component abundances

Abundance maps relative to H^+ were created for the N^+, O^+, O^{2+}, S^+, S^{2+}, Ar^{2+} ions, using the narrow λλ6584, 7320+7330, 5007, 6717+6730, 6312 and 7136 Å lines, respectively (via the ABUND task in IRAF). Each VIMOS spaxel was treated as a distinct 'nebular zone' with its own set of physical conditions. Ionic argon and sulphur abundance ratios were converted to total Ar/H and S/H using an ICF(Ar) = 1.87 and ICF(S) = 1.03, respectively (Kingsburgh & Barlow 1994). Very small changes were found by adopting the ICF prescriptions of Izotov et al. (2006). Since T_e maps are unattainable for the narrow component gas, we have adopted the upper limit of T_e = 10 000 K applicable throughout Mrk 996 (Section 4.1), together with the mean electron densities derived from the [S II] doublet ratios, of 170 and 10 cm^{-3} for the inner core and outer region, respectively (Table 3). It is emphasized that since the adopted T_e for the narrow component gas is an upper limit, the abundances derived here are necessarily lower limits. In Fig. 16 abundance distributions are shown in the directions from north-east to south-west and south-east to north-west that pass through the centre of Mrk 996 (i.e. in the X and Y directions across the abundance maps, respectively, produced by averaging over a three spaxel-wide pseudo-slit). The variations in the abundances of O^{2+} and O^+ in Fig. 16 mirror each other in their distribution. As expected, the more highly ionized species is dominant in the core region, where the UV radiation is expected to be harder. It should further be noted that these abundance trends are only correct if the temperature is constant throughout the gas emitting the narrow line component.

The O/H elemental ratio was derived by summing the O^+ and O^{2+} ionic abundance maps. Adopting a solar oxygen abundance of 4.9×10^{-4} relative to hydrogen (Allende Prieto, Lambert & Asplund 2001), we find that Mrk 996 has an oxygen abundance of ≥0.50 solar throughout the inner core region and beyond. This is a significantly higher metallicity than the ∼0.2 solar derived previously by TIL96, which can be attributed to the high electron temperature of 15 000 K that they employed, based on CLOUDY models.

An N/H abundance ratio map (Fig. 17) was created using an ionization correction factor, $ICF(N) = (O^+ + O^{2+})/O^+$ (Kingsburgh & Barlow 1994). Again, very small changes were found by adopting the ICF prescriptions of Izotov et al. (2006). For a constant electron temperature, the N/H ratio, shown in Fig. 17, remains constant throughout the core at $\geq 0.8 \times 10^{-5}$ but shows a two-fold increase north-east of the core region of Mrk 996. A cut across the N/O ratio map of Mrk 996, which is much less sensitive to the adopted electron temperature than either O/H or N/H, shows a similar trend, with log(N/O) ≃ −1.5 in the core, rising to ≃ −1.2 at a spot north-east

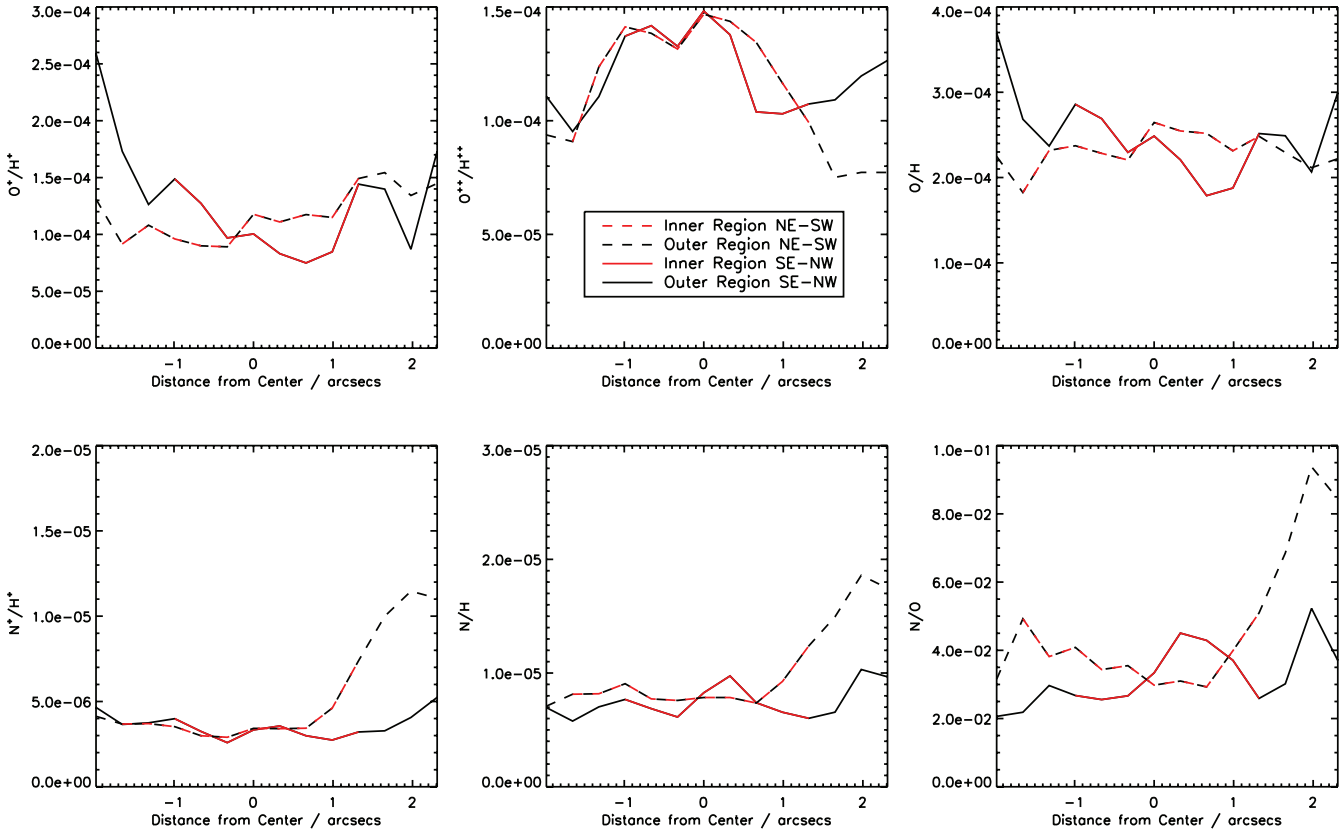

Figure 16. Spatial variations in narrow component ionic and elemental abundances across Mrk 996 obtained for T_e = 10 000 K and N_e = 170 cm^{-3}. The available T_e is an upper limit so the abundances shown are lower limits. The patterns should persist if T_e is constant across the emitting region. Three spaxel-wide averages were made across the IFU aperture in its X and Y directions, corresponding to south-east to north-west and north-east to south-west, respectively.

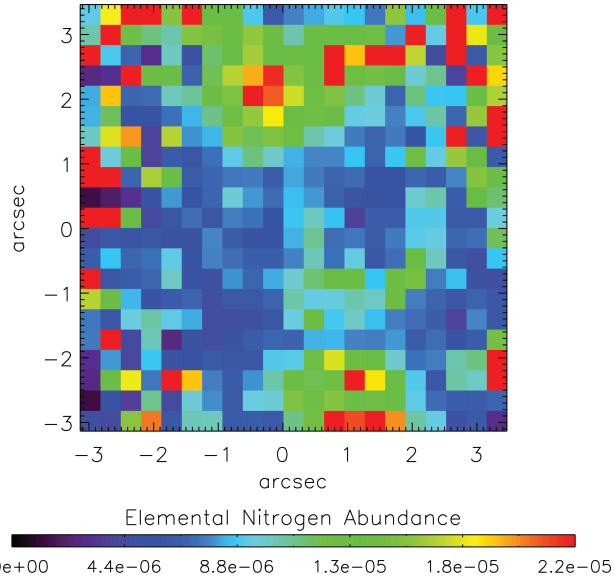

Figure 17. N/H abundance ratio map based on the narrow component emission across the region where [N II] λ6584 is seen. It should be noted that these abundances are lower limits since an upper limit to T_e was used for the calculation.

Table 4. Adopted abundances for the narrow (C1) and broad (C2) component emission regions throughout Mrk 996.

	C1	C2
Adopted T_e (K)	10 000[a]	11 000
Adopted N_e (cm^{-3})	170	10^7
He/H	0.091 ± 0.017	0.072 ± 0.018
$N^+/H^+ \times 10^5$	0.46 ± 0.18	4.1 ± 1.1
$N^{2+}/H^+ \times 10^4$	–	1.3 ± 0.5
$N/H \times 10^5$	0.89 ± 0.25	17.0 ± 7.6[b]
$O^+/H^+ \times 10^4$	1.3 ± 0.4	–
$O^{2+}/H^+ \times 10^4$	1.1 ± 0.2	2.0 ± 0.2
$O/H \times 10^4$	2.4 ± 0.4	2.3 ± 1.1[b]
$S^+/H^+ \times 10^7$	10.3 ± 1.8	(9.7 ± 1.8)
$S^{2+}/H^+ \times 10^6$	4.7 ± 0.9	5.4 ± 1.3
$S/H \times 10^6$	5.9 ± 1.6	6.6 ± 1.6
$Ar^{2+}/H^+ \times 10^7$	8.19 ± 1.8	12.0 ± 2.8
$Ar/H \times 10^6$	1.5 ± 0.3	2.2 ± 0.5
log N/O	−1.43	−0.13
log S/O	−1.61	−1.54
log Ar/O	−2.20	−2.02

[a]Upper limit adopted T_e so that C1 abundances are lower limits.
[b]Applicable to a central 0.86 arcsec (FOS) aperture; see the text for details.

of the core (Fig. 16). The mean abundances are listed in Table 4. For the revised oxygen metallicity of Mrk 996 the derived N/O, S/O and Ar/O ratios fall within the expected range for BCDs (e.g. Izotov et al. 2006).

5.2 Broad component abundances

In order to derive nitrogen elemental abundance for the broad component gas, we correct for the presence of N^{2+} using the N III] λ1750 line detected by *HST* FOS. This high excitation energy UV line was not used to correct the narrow emission component nitrogen abundances because it ought to originate from the high excitation gas responsible for the *broad* line emission. Table 5 lists the ionic abundances derived for the broad line emission gas derived from optical and UV lines. Fluxes are quoted relative to the broad Hβ flux within the simulated FOS aperture and are corrected for extinction using the average $c(H\beta)$ value within that aperture in the reddening map derived from the broad components of Hα/Hβ, Hγ/Hβ ratios. The physical conditions adopted for these calculations are those derived from the broad component emission, i.e. $T_e = 10\,000 \pm 3500$ K and $\log(N_e/\mathrm{cm}^{-3}) = 7.25^{+1.25}_{-0.75}$. We consider that the highest allowed T_e is 11 000 K with $\log(N_e/\mathrm{cm}^{-3}) = 7.00$ being the lowest allowed density, based on Fig. 15(c). This latter density is consistent with the upper density limit inferred from the [Fe III] diagnostics. For $T_e = 11\,000$ K and $\log(N_e/\mathrm{cm}^{-3}) = 7.00$ the resulting broad line O/H abundance ratio of 2.3×10^{-4} is consistent with being the same as for the narrow line emission regions (cf. Tables 4 and 5). As a consistency check, we determined the T_e for the narrow component VIMOS [O III] λ5007 and Hβ fluxes falling within the FOS aperture that would be required to match the above broad line O/H ratio. This yielded a temperature of ∼9200 K, reinforcing the upper limit of 10 000 K derived in Section 4.1 for the C1 emission. S/H abundances were computed using the [S III] λ6312 line and an estimated (minor) contribution from S^+/H^+ (in parentheses in Table 4) using equation (A38) of Kingsburgh & Barlow (1994). Ar/H abundance ratios were derived using the [Ar III] λ7136 line with ICF(Ar) = 1.87 as previously. The adopted mean values are listed in Table 4.

In contrast to the apparent lack of significant variation in the abundances of oxygen, sulphur and argon between the two velocity components, it appears that the N/O ratio in the broad line region is enriched by a factor of ∼20 relative to the narrow line region, with the broad line region having log(N/O) ∼ −0.13. We conclude that the observations are consistent with the narrow and broad line regions both having an O/H ratio of ≥0.5 solar.

5.3 Elemental helium abundance

Narrow and broad component He^+/H^+ abundance maps were derived from He I λ5876 C1 and C2 maps. Abundances were calculated using the Case B He I emissivities of Porter et al. (2005) at the respective T_e and N_e of the broad and narrow emission components. Since these are only valid up to $\log(N_e/\mathrm{cm}^{-3}) = 6$, a correction factor of 0.9543 was applied to the broad component emissivity to extrapolate up to $\log(N_e/\mathrm{cm}^{-3}) = 7.25$. At these densities, collisional excitation from the $He^0 2s^3S$ metastable level by electron impacts contributes to the observed broad He I λ5876 component; this effect is accounted for by Porter et al. (2005). Fig. 18 shows *X* and *Y* direction cuts across the broad and narrow component elemental He/H maps. We have assumed that the He^{2+}/H^+ fraction is negligible. Good agreement between the spatial variations in the He/H abundance for each component is observed. No relative He/H enrichment is seen across the components; within the uncertainties both fall between the pre-galactic He/H ratio of 0.08 (Luridiana et al. 2003) and the solar ratio 0.10 (Lodders 2003). This contrasts with the localized N/H enrichment north-east from the nucleus that spatially correlates with a peak in equivalent width (EW)(Hβ) (see Section 6). The slight decrease in He/H in the core region might be attributable to the presence of He^{2+}. We find this unlikely, however, since no nebular He II λ4686 emission has been detected (none was reported in the recent study by Thuan, Hunt & Izotov 2008), and in addition, other similarly high excitation lines such as [Ar IV] are not present in the spectrum of the galaxy. The derived He/H abundances at the centre of Mrk 996 agree well with those of TIL96 who

Table 5. Intensities of UV emission lines from *HST* FOS spectra and their optical broad component counterparts, measured within a FOS aperture superimposed on our broad component flux maps. All intensities are given relative to the broad component $F(\mathrm{H}\beta) = 122.1 \pm 11.1 \times 10^{-15}$ erg s^{-1} cm^{-2} within the simulated aperture.

			Abundance $\times 10^4$		
		T_e/K	9000	10 000	11 000
		log (N_e/cm^{-3})	7.50	7.25	7.00
Line	$100 \times I(\lambda)/I(\mathrm{H}\beta)$	Species			
5755 [N II]	7.1 ± 1.9	N^+/H^+	1.9 ± 0.5	0.9 ± 0.2	0.4 ± 0.1
1750 N III]	19.2 ± 6.8	N^{2+}/H^+	7.5 ± 2.6	3.0 ± 1.1	1.3 ± 0.5
		N/H	9.4 ± 1.3	3.8 ± 1.7	1.7 ± 0.8
5007 [O III]	51.3 ± 6.2	O^{2+}/H^+	12.6 ± 1.5	4.8 ± 0.6	2.0 ± 0.2
		O/H	15.7 ± 7.5	5.5 ± 2.6	2.3 ± 1.1

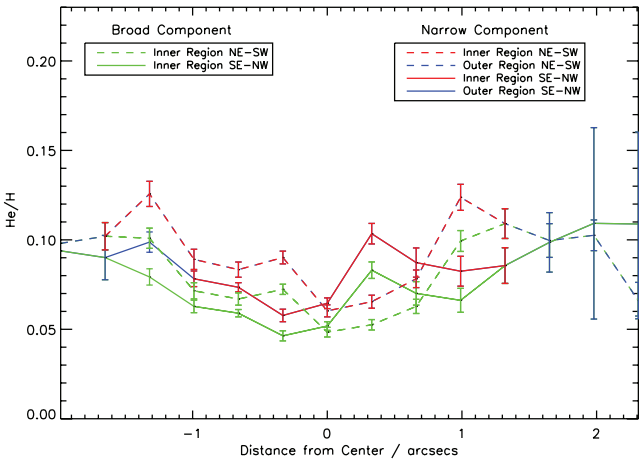

Figure 18. Spatial variations in the narrow (blue and red) and broad (green) component He/H elemental abundance across Mrk 996. Three spaxel-wide averages were made across the IFU aperture in its *X* and *Y* directions, corresponding to the south-east to north-west and north-east to south-west, respectively.

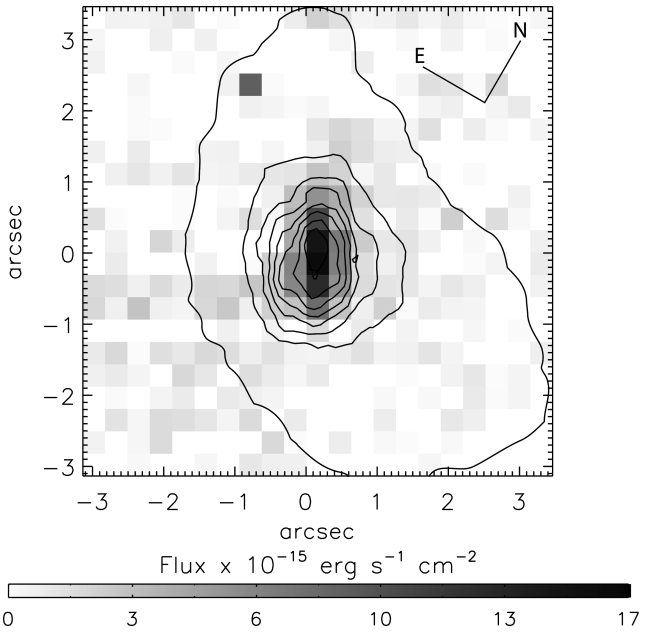

Figure 19. Emission map of the blue WR feature (created by integrating over the full emission feature and removing contaminant flux from [Fe III] λ4658), showing the distribution of WR stars in the inner core region of Mrk 996. Overlaid are the Hα narrow component flux contours from Fig. 1.

calculated $He^+/H^+ \sim 0.09$ from the He I λ5876 emission within their FOS aperture.

Table 4 summarizes the derived abundance for the narrow and broad line emission regions of the galaxy.

6 WOLF–RAYET STARS AND STELLAR AGE

WR features were identified in Mrk 996 by TIL96 in their single aperture FOS spectroscopy of a 0.86-arcsec region at the centre of Mrk 996. The VIMOS IFU spectra also show a broad WR stellar feature at 4650 Å, attributable to a mixture of late-type WN (WNL) and WC stars at He II λ4686 and N III λ4640 (with an additional weak WC stellar C IV feature at 5808 Å). The WR spectral signatures are seen to extend throughout the core region of Mrk 996 and show excellent agreement with the spatial extent of the broad [O III] λ4363 emission (Fig. 8). A map of the 4650 Å WR feature is shown in Fig. 19; this has been decontaminated from the emission by nebular [Fe III] λ4658 by fitting a Gaussian profile to the line and subtracting its flux from the integrated flux of the 4650 Å feature. After summing the spectra over the core region, Large Magellanic Cloud (LMC) WR spectral templates from Crowther & Hadfield (2006) were used to fit both spectral features (Fig. 20). Although the WC feature is weak, its contribution is essential in fitting the broad wings of the 4650 Å feature. At the distance of Mrk 996 (22 Mpc) the two WR features indicate the presence of ∼2600 WNL stars and ∼400 WC stars. Assuming a similar depth for the area over which these spectral features are summed, 1.7×2.3 arcsec^2 (4.6×10^4 pc^2), results in a volume density of 3×10^{-4} WR stars per pc^3 in the core region.

We can compare our WR number estimates with those of TIL96, who estimated that 600 late-type WN stars and 74 WC stars were responsible for the WR emission seen within their 0.86-arcsec diameter FOS aperture. Scaling our own core region WR number estimates for the difference in aperture size would predict 390 WNL stars and 60 WC stars within the FOS aperture. While the agreement between the two estimates is quite good, the decrease in WNL star numbers for our scaled estimate can be attributed to the non-uniform density of WR stars in the core region (see Fig. 19). In contrast, the WC 5808 Å feature is very centrally peaked, thus giving a good agreement between the two estimates.

Luminosities of hydrogen recombination lines, particularly Hβ, can provide estimates of the ionizing flux present, assuming a radiation-bounded nebula (Schaerer & Vacca 1998). Thus, the EW of Hβ is commonly used as a stellar age indicator at a given

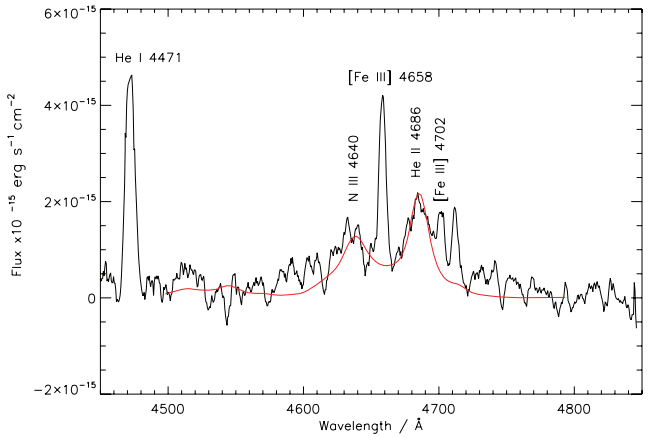

Figure 20. WR 'blue bump' feature summed over the inner core of Mrk 996. Overplotted is the combined fit for 2600 WNL stars and 400 WC stars, using the templates of Crowther & Hadfield (2006).

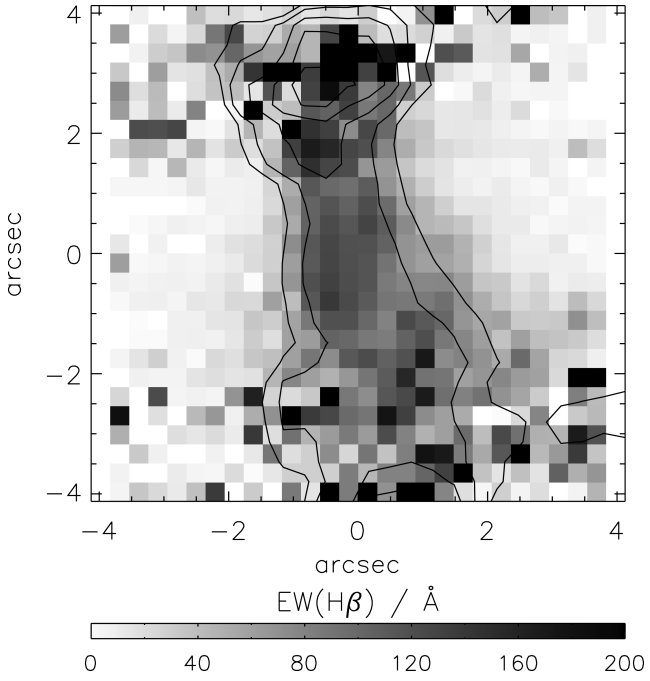

Figure 21. Map of the EW of Hβ across Mrk 996, derived from the full emission line profile. Contours range from 70 to 180 Å in steps of 30 Å.

metallicity. A map of EW(Hβ) across Mrk 996 (derived from integrating over the full emission line profile) is shown in Fig. 21 and displays a surprising morphology compared to the central location of the ionizing sources in Mrk 996. A peak is seen directly north-east of the centre of the galaxy, which correlates well with the peak in [N II] λ6584 emission shown in Fig. 17. We can use the EW(Hβ) map, in conjunction with the metallicity map (described in Section 5.1), to estimate the distribution of stellar ages throughout Mrk 996. We find that the core region EW(Hβ) corresponds to a stellar age of 4.5 Myr whereas the EW(Hβ) peak north-east of the core corresponds to a slightly younger stellar age of $\sim$3 Myr (cf. fig. 7 of Schaerer & Vacca 1998); these ages are sufficiently long to allow for the presence of WR stars in the galaxy.

An estimation of the number of O-type stars was made, assuming that all ionizing photons, $Q_0^{\rm obs}$, are produced by O and WR stars and utilizing the Hβ luminosity, L(Hβ), integrated over the whole galaxy (i.e. using the dereddened combined C1 and C2 Hβ flux from the inner and outer regions, and at a distance of 22.3 Mpc). The absolute number of O stars was derived using (e.g. Fernandes et al. 2004)

$$N_{\rm O} = N_{\rm OV} = \frac{Q_0^{\rm obs} - N_{\rm WR} Q_{\rm WR}}{\eta_0(t) Q_{\rm O7V}}, \quad (1)$$

where $Q_0^{\rm obs}$ is the emission rate of ionizing photons, as derived from L(Hβ), and $Q_{\rm WR}$, $Q_{\rm O7V}$ are the emission rates of ionizing photons by WR stars and O7V stars, respectively, with $N_{\rm WR}$ being the total number of WR stars. $\eta_0(t)$ is a conversion parameter for the proportion of O7V stars relative to all OV stars and is estimated as being $\geq$0.2 by Schaerer & Vacca (1998) at the metallicity of Mrk 996 ($\sim$0.5 $Z_\odot$). Adopting $\eta_0(t) = 0.2$, $Q_{\rm WR} = Q_{\rm O7V} = 1.0 \times 10^{49}$ s^{-1} (Schaerer, Contini & Kunth 1999) and $Q_0^{\rm obs}$(C1 + C2) = 3.36 $\times$ 10^{53} photons s^{-1} we find $N_{\rm O} \lesssim 153\,000$ yielding $N_{\rm WR}/N_{\rm OV} \gtrsim 0.02$. As a lower limit, this ratio is in good agreement with those predicted by evolutionary synthesis models by previous studies; at the predicted age of <5 Myr for the Mrk 996 SB, Cerviño & Mas-Hesse (1994) find that this $N_{\rm WR}/N_{\rm OV}$ fraction is typical at metallicities of 0.4 $Z_\odot$, while Schaerer & Vacca (1998) predict $N_{\rm WR}/(N_{\rm WR} + N_{\rm O}) = 0.04$ for a metallicity of 0.25 $Z_\odot$.

Using the Hα–SFR (star formation rate) relation of Kennicutt (1998) and the total Hα luminosity (C1+C2) of 4.83 $\times$ 10^{41} erg s^{-1} we obtain a global current SFR of 3.8 $M_\odot$ yr^{-1}. Taking into account the subsolar metallicity of Mrk 996 this can be reduced to 2.7 $M_\odot$ yr^{-1} (Lee et al. 2002). However, in the event that the C2 component emission is partly attributable to shock-excited gas (see Section 7.1) so that it cannot be included in the estimate of $Q_0^{\rm obs}$, a SFR lower limit of 1.3 $M_\odot$ yr^{-1} is derived based on Q_0(C1) = 1.31 $\times$ 10^{52} photons s^{-1} alone.

7 DISCUSSION

7.1 Diagnosing the ionization mechanisms

In order to gain insight into the mechanisms responsible for the multicomponent line emission from Mrk 996, we made use of the classic diagnostic diagrams of Baldwin, Phillips & Terlevich (1981) (the BPT diagrams). These are employed to classify galaxies according to the dominant excitation mechanism of their emission lines, i.e. either photoionization by massive stars within H II regions or photoionization by non-thermal continua from active galactic nuclei (AGN). The diagrams consist of excitation-dependent, extinction-independent line ratios: log([O III] λ5007/Hβ) versus either log([N II] λ6584/Hα) or log([S II](λ6716, 6731)/Hα). SFG fall into the lower left region of the diagram, AGN host galaxies fall into the upper right region and Low-Ionization Nuclear Emission Line Regions (LINERs) fall in the lower right region. The separation is not as clear, however, for low metallicity AGN (see e.g. Stasińska et al. 2006), only a handful of which have been proposed to exist thus far (Izotov & Thuan 2008).

Kewley et al. (2001) calculated the first SB grids that attempted to match optical diagnostic diagrams based on purely empirical data, by coupling the MAPPINGS III photoionization code and STARBURST99 population synthesis models. Whereas previous semi-empirical studies involved only solar metallicity calculations, their line ratios were computed for a range of metallicities (Z = 0.05–3.0 $Z_\odot$) and ionization parameters (q = 5 $\times$ 10^6–3 $\times$ 10^8 cm s^{-1}), where q

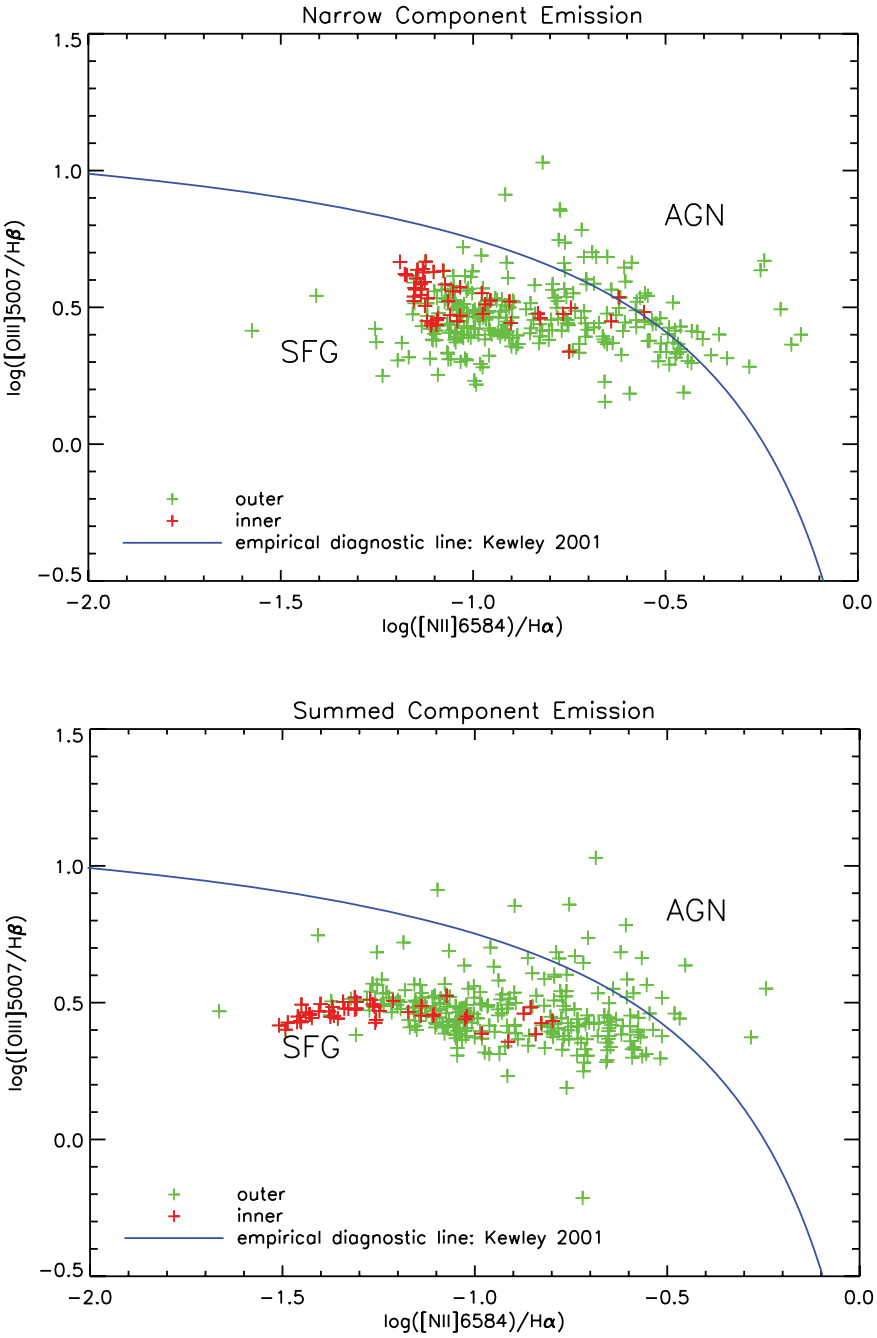

Figure 22. Emission line diagnostic diagram for Mrk 996. Each data point represents a spaxel in the ratioed dereddened flux maps corresponding to [O III] λ5007/Hβ and [N II] λ6584/Hα. The empirical diagnostic 'maximum SB' line from Kewley et al. (2001) is also shown, as are the positions of emission line ratios for SFG and AGN. The top panel represents narrow component emission line map ratios whereas the bottom panel shows ratios derived from the full emission line profile (i.e. narrow + broad component emission, where detected).

is the maximum velocity of an ionization front that can be driven by the local radiation field and is related to the non-dimensional ionization parameter $U = q/c$ (Dopita et al. 2001). Utilizing these grids, Kewley et al. (2001) determined a 'maximum SB line' (shown in Fig. 22), above which the flux ratios of an object cannot be fitted by pure SB models alone. Ratios lying above this photoionization boundary require additional sources of excitation such as shocks or AGN. As mentioned above, this picture has recently been revised and it is now believed that low-Z AGN, should they exist, would occupy similar regions on the BPT diagram as normal H II galaxies; based on an analysis of a large sample of Sloan Digital Sky Survey galaxies, Stasińska et al. (2006) have found that composite AGN/H II region models with $Z < 0.4\,Z_{\odot}$ lie very close to and below the pure H II region sequence, whereas when considering also the regime of $Z > 0.6\,Z_{\odot}$ they established that the locus below the Kewley et al. (2001) line allows for an AGN-excited gas component of up to 20 per cent.

It is therefore instructive to see what area of the BPT diagram Mrk 996 occupies. Kewley et al. (2001) found that since the [S II](λ6716, 6731)/Hα ratio is affected by the density of the line

emitting region and it is therefore less accurate as a diagnostic. Hence considering the large density difference between the narrow and broad component gas within Mrk 996 we only considered the [O III] λ5007/Hβ versus [N II] λ6584/Hα ratios (Fig. 22). Since no broad component is detected for [N II] λ6584 we have not been able to create separate broad and narrow diagnostic diagrams and instead present (i) a narrow component diagram (Fig. 22, top panel), and (ii) ratios derived from the entire emission line profiles (i.e. integrated over broad and narrow component emission, where both exist; Fig. 22, bottom panel). Spaxels corresponding to the core region of the galaxy are shown as red crosses, with outer region spaxels plotted as green crosses. Also shown is the maximum SB line of Kewley et al. (2001).

The data points for the outer narrow line region of Mrk 996 mostly straddle the 'theoretical' upper limit for pure photoionization. Based on the Kewley et al. (2001) grids, the flux ratios lie within a metallicity range of $Z = 0.3$–0.5 and along and above an ionization parameter track for $q = 3 \times 10^8$ (the maximum ionization parameter computed). The narrow component emission in the core region occupies the top left of the distribution, which corresponds to a higher ionization parameter and lower metallicity in the SB grids, while a significant number of data points fall outside the SFG area of the plot. When the broad component is included in the diagnostics, the location of the outer region spaxels move to the left, whereas the core region spaxels move downwards and to the left for both ratios to occupy a lower ionization parameter and metallicity region. This is most likely due to the suppression of the [O III] λ5007 broad component emission within the high-density core region, which would lower the combined narrow plus broad [O III] λ5007/Hβ ratio.

As previously mentioned, exceeding the 'maximum SB' line can also be indicative of a contribution to the ionization by fast shocks. However, the amount by which this line can be crossed before shocks must be a substantial source of ionization has not been established thus far. Similar diagrams were created by Calzetti et al. (2004) for four SB galaxies using ratios from *HST* WFPC2 images, such as [O III] λ5007/Hβ versus [S II] λ6716, 6731/Hα. They found that a number of regions in the SB galaxies lay above the maximum SB line and as a result defined regions of non-stellar excitation as either lying above and to the right of it or where the [S II]/Hα ratio is high enough to be compatible with non-stellar sources, i.e. [S II]/H $\alpha >$ 0.7–0.9 (Shull & McKee 1979; Veilleux & Osterbrock 1987). The log([S II] λ6716, 6731/Hα) ratio is traditionally used as a diagnostic for shock-excited gas because shock models predict that relatively cool high-density regions should form behind the shock front and emit strongly in [S II] (Dopita 1978). The [S II]/Hα flux ratios for the narrow component emission across Mrk 996 lie between 0.03 and 6×10^{-4}, well below the high [S II]/Hα ratios predicted for shocks. On the other hand, Thuan et al. (2008) employed a model with shocks at a velocity of 250 km s^{-1} that reproduced the observed intensity of the high-ionization potential [O IV] 25.9 μm line detected in the *Spitzer* spectrum of Mrk 996. In conclusion, Fig. 22 by itself cannot provide firm evidence for or against the presence of AGN activity within Mrk 996 given the galaxy's rather low metallicity status, even though the integrated broad component Hα luminosity of 2.5×10^{41} erg s^{-1} this at the lower limit of those measured from rare low-Z BCDs suspected of harbouring AGN (3×10^{41}–2×10^{42} erg s^{-1}; Izotov & Thuan 2008). Although photoionization appears to be the dominant excitation mechanism, we cannot rule out a contribution from shocks, particularly with respect to the broad component emission. We draw attention to the significant bias inherent in BPT diagrams of galaxies whose analysis does not involve a separate consideration of narrow/broad line diagnostics.

7.2 What is the origin of the broad line emission?

Mrk 996 is not the only BCD that shows evidence for large linewidths. Izotov, Thuan & Guseva (2007) presented an analysis of a large number of low metallicity BCDs exhibiting broad emission lines with inferred gas expansion velocities of 1000–7000 km s^{-1}. WR stellar winds have been proposed as a possible mechanism for producing such broad linewidths, but thus far no correlation between the presence of broad nebular lines and broad WR features have been found (Izotov et al. 2007). We find that in Mrk 996 the surface brightness of the 4650 Å WR feature does not correlate tightly with that of [O III] λ4363 (Fig. 23), further indicating that the mechanism responsible for the broad line emission is not active only in the regions where WR stars are present.

Roy et al. (1991, 1992) investigated a variety of mechanisms to explain broad nebular gas components in H II regions, including electron scattering, stellar winds, supernova remnants and superbubble blowouts. However, each of these mechanisms was deemed unsatisfactory. An exploration of blowout mechanisms

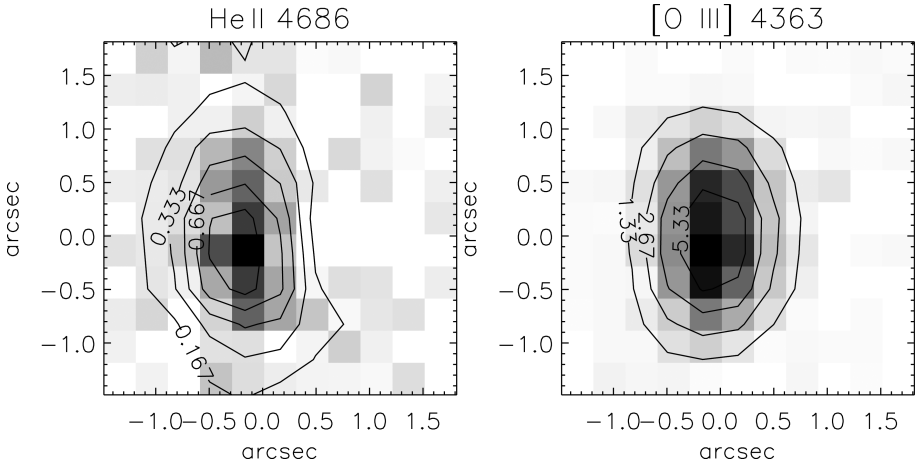

Figure 23. Grey-scale and contour emission line maps of the He II λ4686 WR feature (left-hand panel) and nebular [O III] λ4363 (right-hand panel). Their contours suggest that the ionization mechanism responsible for the broad emission line components (represented by [O III] λ4363) may not be strictly due to the WR stars. Flux contours are in units of $\times 10^{-15}$ erg s^{-1} cm^{-2} per 0.33 × 0.33 arcsec^2 spaxel.

within low-metallicity H II regions was conducted by Tenorio-Tagle et al. (1997) using a hydrodynamical calculation to try to match a sample of low-metallicity H II regions with broad emission line components. They proposed that the absence of strong radiative cooling in the low-metallicity ISM within these regions could delay the action of Rayleigh–Taylor (RT) instabilities that can fragment the expanding shell within a blowout. However, this mechanism may not be applicable to Mrk 996, as one of the required conditions is a low-density environment, whereas we derive high densities for its broad component gas [$\log(N_e/\mathrm{cm}^{-3}) \sim 7$].

Broad line emission (FWHM $\approx 400\,\mathrm{km\,s^{-1}}$; C2) is detected throughout the central regions of Mrk 996, throughout the bright SB region and out to >5 arcsec. Close to the nucleus of the galaxy the broad Balmer line component splits into two additional *broad* components (FWHM $\approx$ 200–300 $\mathrm{km\,s^{-1}}$) which trace the kinematics of a two-armed mini spiral, but component C2 does not show evidence of velocity splitting at our level of spectral resolution farther out (Figs 3 and 4). Given the youth of the SB region in Mrk 996 (<5 Myr) containing large numbers of young O- and WR-type stars (Section 6), and presence of very dense zones of gas (Section 4.3), it is possible that the broad line emission partly originates from a turbulent mixing layer forming on the surface of dense cool clumps which are subjected to irradiation and hydrodynamic ablation from the hot winds from young massive star clusters (Begelman & Fabian 1990; Slavin, Shull & Begelman 1993). Recent work on the nearby NGC 1569 and M82 has revealed that the broad line component observed in those SB galaxies can be explained as originating within turbulent layers on the surface of the dense gas clumps (Westmoquette et al. 2007a,b). Motivated by this hypothesis, Binette et al. (2009) have successfully modelled the broad underlying components seen in the Balmer and [O III] lines of NGC 2363 via the inclusion of a turbulent mixing layer and conclude that the broad profile results from radial acceleration of photoionized turbulent gas. Their models also correctly predict the absence of a broad component in [S II] and [N II] lines. Although the applicability of these results to Mrk 996 may be limited due to the high densities of Mrk 996's broad components ($N_e = 100\,\mathrm{cm}^{-3}$ is adopted for NGC 2363) and their much broader predicted linewidths ($\pm 3500\,\mathrm{km\,s^{-1}}$), their results lend a great deal of weight to the turbulent mixing layer hypothesis.

This mechanism could also be at work here. It is probable that the central region of Mrk 996 consists of many small, dense clouds of relatively low volume filling factor dispersed within the young star clusters of the SB. This results in a large cloud surface area with which the copious ionizing photons and fast stellar winds can interact. If the presence of broad emission indicates that strong wind–clump interactions are taking place, then by extension, material from these interaction sites must be being stripped off and entrained into the cluster wind flows contributing to the overall appearance of component C2.

8 SUMMARY AND CONCLUSIONS

Mrk 996 is a complex system containing an extended SB region (216–432 pc in radius) with a centrally concentrated WR population in the nuclear regions ($\lesssim$200 pc). The young stellar population in the nuclear supercluster contains ~3000 WR stars and $\lesssim$150 000 O7V-type equivalent stars. The age of the nuclear SB is estimated to be ~4.5 Myr but there is evidence that the extended SB is younger by ~1 Myr. The presence of an old stellar population ($\gtrsim$1 Gyr) has been independently established (Thuan et al. 2008). The current star formation rate is $\sim 2\,\mathrm{M_\odot\,yr^{-1}}$. The spatially mapped ionized gas shows a composite emission spectrum consisting of narrow and broad lines. The Balmer line velocity structure close to the nucleus confirms the presence of a spiral structure confined in the inner 160 pc. The Hα broad component has a large integrated luminosity of $2.5 \times 10^{41}\,\mathrm{erg\,s^{-1}}$; this is at the lower limit of those measured from the rare low-Z BCDs suspected of harbouring AGN (Izotov & Thuan 2008). Our VIMOS IFU analysis has enabled a separate analysis of the physical conditions and chemical composition of the narrow and broad emission line regions. The broad line region in the nuclear SB is very dense ($10^7\,\mathrm{cm}^{-3}$) whereas the narrow line component is of lower density ($\lesssim 10^3\,\mathrm{cm}^{-3}$).

The upwards revised oxygen metallicity of Mrk 996 is $\geq 0.5\,\mathrm{Z_\odot}(12 + \log \mathrm{O/H} \approx 8.37)$. The broad line region is nitrogen enriched compared to the narrow line region by $\lesssim$1.3 dex. However, no relative enrichment of He, O, S and Ar is inferred. The S/O and Ar/O abundance ratios in the two components, as well as the N/O ratio in the *narrow* line component, are typical of those in H II galaxies and dwarf irregulars (e.g. Izotov et al. 2006; van Zee & Haynes 2006). The narrow line N/O ratio in particular is exactly the value expected based on the galaxy's colour, and follows the metallicity–luminosity relationship for isolated dwarf galaxies (cf. figs 8 and 9 of van Zee & Haynes 2006, for $M_B = -16.7$, $B - V = 0.44$; TIL96); its mean current value can be interpreted as the result of the slow release of nitrogen from the intermediate-mass stellar population over the last few Gyr. On the other hand, the high N/O ratio in the broad line region of the inner galaxy is consistent with the presence of numerous evolved massive stars (e.g. WNL-type and luminous blue variables) and can be attributed to the cumulative effect of their N-enriched winds. An elevated N/O could not in this case be due to the outflow of oxygen-enriched gas from supernova explosions: the absence of elevated (or suppressed) O/H, S/H and Ar/H ratios in the broad line gas implies that recent supernova ejecta are probably not implicated in its excitation; at the young age of the Mrk 996 SB only a few very massive stars ($\gtrsim 50\,\mathrm{M_\odot}$) would have exploded as supernovae (e.g. Woosley, Heger & Weaver 2002). The mild two-fold increase over the mean of the narrow line N/H (Fig. 17) spatially correlates with a local peak in EW(Hβ) in a region (Fig. 21) where no WR stars are seen. This could mean that even though the narrow line gas is fairly well mixed, some localized N-enrichment has already occurred in an area dominated by normal OB-type stars which is slightly younger than the nuclear SB.

Finally, we would like to draw attention to the nature of the broad [O III] λ4363 line detected in Mrk 996. Even though this galaxy represents an extreme case in harbouring a very dense ionized component which dominates the excitation of this line, it is by no means unique (see e.g. Izotov et al. 2007). In such cases where a substantial fraction of the [O III] 4363 and 4959, 5007 Å lines arise in different gas components, the integrated auroral to nebular ratio would *not* be representative of the electron temperature of the overall H II region; using it would result in biased physical conditions and chemical abundances. The problem would be aggravated in analyses based on low dispersion, low spatial resolution spectra and may therefore have implications for the so-called 'heating problem' of blue compact galaxies (e.g. Stasińska & Schaerer 1999; Péquignot 2008).

ACKNOWLEDGMENTS

We thank the VIMOS support staff at Paranal for taking these service mode observations [programme 078.B-0353(A), PI: Tsamis]. We appreciate discussions with Marina Rejkuba and Carlo Izzo about the VIMOS instrument and the GASGANO reduction pipeline.

Also, our thanks go to Fabrizio Sidoli for helpful discussions regarding WR template spectra and to Nate Bastian for advice on IFU cube construction. This research has made use of the NASA ADS data base. BLJ acknowledges support from a STFC studentship. YGT acknowledges support from a STFC fellowship and from grants AYA2007-67965-C03-02 and CSD2006-00070 CONSOLIDER-2010 'First science with the GTC' of the Spanish Ministry of Science and Innovation.

REFERENCES

Allende Prieto C., Lambert D. L., Asplund M., 2001, ApJ, 556, L63
Baldwin J. A., Phillips M. M., Terlevich R., 1981, PASP, 93, 5
Bastian N., Emsellem E., Kissler-Patig M., Maraston C., 2006, A&A, 445, 471
Begelman M. C., Fabian A. C., 1990, MNRAS, 244, 26P
Binette L., Drissen L., Ubeda L., Raga A. C., Robert C., Krongold Y., 2009, A&A, 500, 317
Calzetti D., Harris J., Gallagher J. S., III, Smith D. A., Conselice C. J., Homeier N., Kewley L., 2004, AJ, 127, 1405
Cerviño M., Mas-Hesse J. M., 1994, A&A, 284, 749
Crowther P. A., Hadfield L. J., 2006, A&A, 449, 711
DeBernardis F., Melchiorri A., Verde L., Jimenez R., 2008, J. Cosmol. Astropart. Phys., 3, 20
Dimeo R., 2005, PAN User Guide. ftp://ftp.ncnr.nist.gov/pub/staff/dimeo/pandoc.pdf
Dopita M. A., 1978, ApJS, 37, 117
Dopita M. A., Kewley L. J., Sutherland R. S., Heisler C. A., 2001, in Tacconi L., Lutz D., eds, Starburst Galaxies: Near and Far. Springer, Berlin, p. 225
Fernandes I. F., de Carvalho R., Contini T., Gal R. R., 2004, MNRAS, 355, 728
Howarth I. D., 1983, MNRAS, 203, 301
Hummer D. G., Storey P. J., 1987, MNRAS, 224, 801
Izotov Y. I., Thuan T. X., 2008, ApJ, 687, 133
Izotov Y. I., Thuan T. X., Lipovetsky V. A., 1994, ApJ, 435, 647
Izotov Y. I., Stasińska G., Meynet G., Guseva N. G., Thuan T. X., 2006, A&A, 448, 95
Izotov Y. I., Thuan T. X., Guseva N. G., 2007, ApJ, 671, 1297
Keenan F. P., Aller L. H., Ryans R. S. I., Hyung S., 2001, Proc. Natl. Acad. Sci. USA, 98, 9476
Kennicutt R. C., Jr, 1998, ARA&A, 36, 189
Kewley L. J., Dopita M. A., Sutherland R. S., Heisler C. A., Trevena J., 2001, ApJ, 556, 121
Kingsburgh R. L., Barlow M. J., 1994, MNRAS, 271, 257
Kunth D., Östlin G., 2000, A&AR, 10, 1
Lee J. C., Salzer J. J., Impey C., Thuan T. X., Gronwall C., 2002, AJ, 124, 3088
Lodders K., 2003, ApJ, 591, 1220
Luridiana V., Peimbert A., Peimbert M., Cerviño M., 2003, ApJ, 592, 846
Moorwood A. F. M., Glass I. S., 1982, A&A, 115, 84
Nazé Y., Rauw G., Manfroid J., Chu Y.-H., Vreux J.-M., 2003, A&A, 408, 171
Péquignot D., 2008, A&A, 478, 371
Porter R. L., Bauman R. P., Ferland G. J., MacAdam K. B., 2005, ApJ, 622, L73
Pustilnik S., Kniazev A., Pramskij A., Izotov Y., Foltz C., Brosch N., Martin J.-M., Ugryumov A., 2004, A&A, 419, 469
Roy J.-R., Boulesteix J., Joncas G., Grundseth B., 1991, ApJ, 367, 141
Roy J.-R., Aube M., McCall M. L., Dufour R. J., 1992, ApJ, 386, 498
Schaerer D., Vacca W. D., 1998, ApJ, 497, 618
Schaerer D., Contini T., Kunth D., 1999, A&A, 341, 399
Schlegel D. J., Finkbeiner D. P., Davis M., 1998, ApJ, 500, 525
Shull J. M., McKee C. F., 1979, ApJ, 227, 131
Slavin J. D., Shull J. M., Begelman M. C., 1993, ApJ, 407, 83
Stasińska G., Schaerer D., 1999, A&A, 351, 72
Stasińska G., Cid Fernandes R., Mateus A., Sodré L., Asari N. V., 2006, MNRAS, 371, 972
Tenorio-Tagle G., Munoz-Tunon C., Perez E., Melnick J., 1997, ApJ, 490, L179
Thuan T. X., Izotov Y. I., Lipovetsky V. A., 1995, ApJ, 445, 108
Thuan T. X., Izotov Y. I., Lipovetsky V. A., 1996, ApJ, 463, 120 (TIL96)
Thuan T. X., Hibbard J. E., Lévrier F., 2004, AJ, 128, 617
Thuan T. X., Hunt L. K., Izotov Y. I., 2008, ApJ, 689, 897
van Zee L., Haynes M. P., 2006, ApJ, 636, 214
van Zee L., Salzer J. J., Skillman E. D., 2001, AJ, 122, 121
Veilleux S., Osterbrock D. E., 1987, ApJS, 63, 295
Walsh J. R., Roy J.-R., 1987, ApJ, 319, L57
Walsh J. R., Roy J.-R., 1989, MNRAS, 239, 297
Walsh J. R., Roy J. R., 1990, in Baade D., Grosbol P. J., eds, ESO Conf. Proc. 34, 2nd ESO/ST-ECF Data Analysis Workshop. ESO, Garching, p. 95
Westmoquette M. S., Exter K. M., Smith L. J., Gallagher J. S., 2007a, MNRAS, 381, 894
Westmoquette M. S., Smith L. J., Gallagher J. S., III, O'Connell R. W., Rosario D. J., de Grijs R., 2007b, ApJ, 671, 358
Woosley S. E., Heger A., Weaver T. A., 2002, Rev. Mod. Phys., 74, 1015
Zanichelli A. et al., 2005, PASP, 117, 1271

This paper has been typeset from a TEX/LATEX file prepared by the author.